# Kinematics of active deformation across the Western Kunlun mountain range (Xinjiang, China), and potential seismic hazards within the southern Tarim Basin.

Christelle Guilbaud, Martine Simoes, Laurie Barrier, Amandine Laborde, Jerome van Der Woerd, Haibing Li, Paul Tapponnier, Thomas Coudroy, Andrew Murray

▶ **To cite this version:**

Christelle Guilbaud, Martine Simoes, Laurie Barrier, Amandine Laborde, Jerome van Der Woerd, et al.. Kinematics of active deformation across the Western Kunlun mountain range (Xinjiang, China), and potential seismic hazards within the southern Tarim Basin.. Journal of Geophysical Research : Solid Earth, 2017, 122 (12), pp.10,398-10,426. 10.1002/2017JB014069 . hal-01668711

**HAL Id: hal-01668711**
**https://hal.science/hal-01668711v1**

Submitted on 21 Aug 2020

**HAL** is a multi-disciplinary open access archive for the deposit and dissemination of scientific research documents, whether they are published or not. The documents may come from teaching and research institutions in France or abroad, or from public or private research centers.

L'archive ouverte pluridisciplinaire **HAL**, est destinée au dépôt et à la diffusion de documents scientifiques de niveau recherche, publiés ou non, émanant des établissements d'enseignement et de recherche français ou étrangers, des laboratoires publics ou privés.

AGU PUBLICATIONS

JGR

Journal of Geophysical Research: Solid Earth

RESEARCH ARTICLE

10.1002/2017JB014069

**Key Points:**
- The structure of the slowly deforming Western Kunlun range is derived from seismic profiles
- A slip rate of 0.5–2.5 mm/yr on the basal thrust fault is determined over the last ~400 kyr from terrace incision
- 2015 $M_w$ 6.4 Pishan earthquake may be an intermediate event if $M_w > 8$ earthquakes rupture the whole frontal decollement

**Supporting Information:**
- Supporting Information S1
- Table S1

**Correspondence to:**
C. Guilbaud,
guilbaud@ipgp.fr

**Citation:**
Guilbaud, C., Simoes, M., Barrier, L., Laborde, A., Van der Woerd, J., Li, H., … Murray, A. (2017). Kinematics of active deformation across the Western Kunlun mountain range (Xinjiang, China) and potential seismic hazards within the southern Tarim Basin. *Journal of Geophysical Research: Solid Earth*, *122*, 10,398–10,426. https://doi.org/10.1002/2017JB014069

Received 3 FEB 2017
Accepted 30 NOV 2017
Accepted article online 4 DEC 2017
Published online 29 DEC 2017

©2017. American Geophysical Union. All Rights Reserved.

# Kinematics of Active Deformation Across the Western Kunlun Mountain Range (Xinjiang, China) and Potential Seismic Hazards Within the Southern Tarim Basin

**Christelle Guilbaud[1], Martine Simoes[1], Laurie Barrier[1], Amandine Laborde[1], Jérôme Van der Woerd[2], Haibing Li[3], Paul Tapponnier[1,4], Thomas Coudroy[1,5], and Andrew Murray[6]**

[1]Institut de Physique du Globe de Paris, Sorbonne Paris Cité, Université Paris Diderot, UMR 7154 CNRS, F-75005, Paris, France, [2]Université de Strasbourg, CNRS, Institut de Physique du Globe de Strasbourg UMR 7516, F-67000, Strasbourg, France, [3]Institute of Geology, Chinese Academy of Geological Science, Beijing, China, [4]Now at Earth Observatory of Singapore, Nanyang Technological University, Singapore, Singapore, [5]Now at Technosol, Ballainvilliers, France, [6]Nordic Laboratory for Luminescence Dating, Aarhus University, Risø DTU, Denmark

**Abstract** The Western Kunlun mountain range is a slowly converging intracontinental orogen where deformation rates are too low to be properly quantified from geodetic techniques. This region has recorded little seismicity, but the recent July 2015 ($M_w$ 6.4) Pishan earthquake shows that this mountain range remains seismic. To quantify the rate of active deformation and the potential for major earthquakes in this region, we combine a structural and quantitative morphological analysis of the Yecheng–Pishan fold, along the topographic mountain front in the epicentral area. Using a seismic profile, we derive a structural cross section in which we identify the fault that broke during the Pishan earthquake, an 8–12 km deep blind ramp beneath the Yecheng–Pishan fold. Combining satellite images and DEMs, we achieve a detailed morphological analysis of the Yecheng–Pishan fold, where we find nine levels of incised fluvial terraces and alluvial fans. From their incision pattern and using age constraints retrieved on some of these terraces from field sampling, we quantify the slip rate on the underlying blind ramp to 0.5 to 2.5 mm/yr, with a most probable long-term value of 2 to 2.5 mm/yr. The evolution of the Yecheng–Pishan fold is proposed by combining all structural, morphological, and chronological observations. Finally, we compare the seismotectonic context of the Western Kunlun to what has been proposed for the Himalayas of Central Nepal. This allows for discussing the possibility of $M \geq 8$ earthquakes if the whole decollement across the southern Tarim Basin is seismically locked and ruptures in one single event.

## 1. Introduction

Convergent plate boundaries are the loci of frequent and destructive earthquakes. This is particularly the case for subduction zones (e.g., Barrientos & Ward, 1990; Chlieh et al., 2007; Simons et al., 2011; Vigny et al., 2011) or mountain ranges such as the Himalayas (e.g., Bilham et al., 2001; Sapkota et al., 2012) or Taiwan (e.g., Dominguez et al., 2003; Simoes, Avouac, & Chen, 2007), where convergence rates are particularly high. There, the first-order characteristics of the seismic cycle of active faults appear to be relatively understood as a result of measurable interseismic deformation from GPS or InSAR (e.g., Ader et al., 2012; Grandin et al., 2012; Hsu et al., 2009) and of existing paleoseismological or historical archives of past earthquakes (e.g., Bollinger et al., 2016; Chen et al., 2004; Hossler et al., 2016; Lavé, 2005). However, such is not the case for slowly converging intracontinental areas where deformation rates are too low to be clearly quantified from usual geodetic techniques (e.g., Godard, Cattin, & Lavé, 2009). The western mountain front of the Andes at the latitude of Santiago in Central Chile (Armijo et al., 2010; Riesner et al., 2017; Vargas et al., 2014) or the LongMen Shan mountain range along the southeastern edge of the Tibetan plateau (Hubbard & Shaw, 2009; Thompson et al., 2015) are such examples. In these cases, our knowledge only relies on thorough geological, structural, and morphological investigations of active tectonics that unfortunately are often only conducted after a destructive earthquake attracted the attention on these particular sites. The 2008 Wenchuan earthquake, within the LongMen Shan, is particularly illustrative of this situation (Hubbard & Shaw, 2009).

Here we focus on one of these slowly deforming continental areas, the Western Kunlun mountain range (Xinjiang, northwest China; Figure 1). Surface geology (e.g., X. Cheng et al., 2016; Matte et al., 1996), seismic reflection profiles (Jiang, Li, & Li, 2013), teleseismic data (e.g., Kao et al., 2001; Qiusheng et al., 2002; Wittlinger

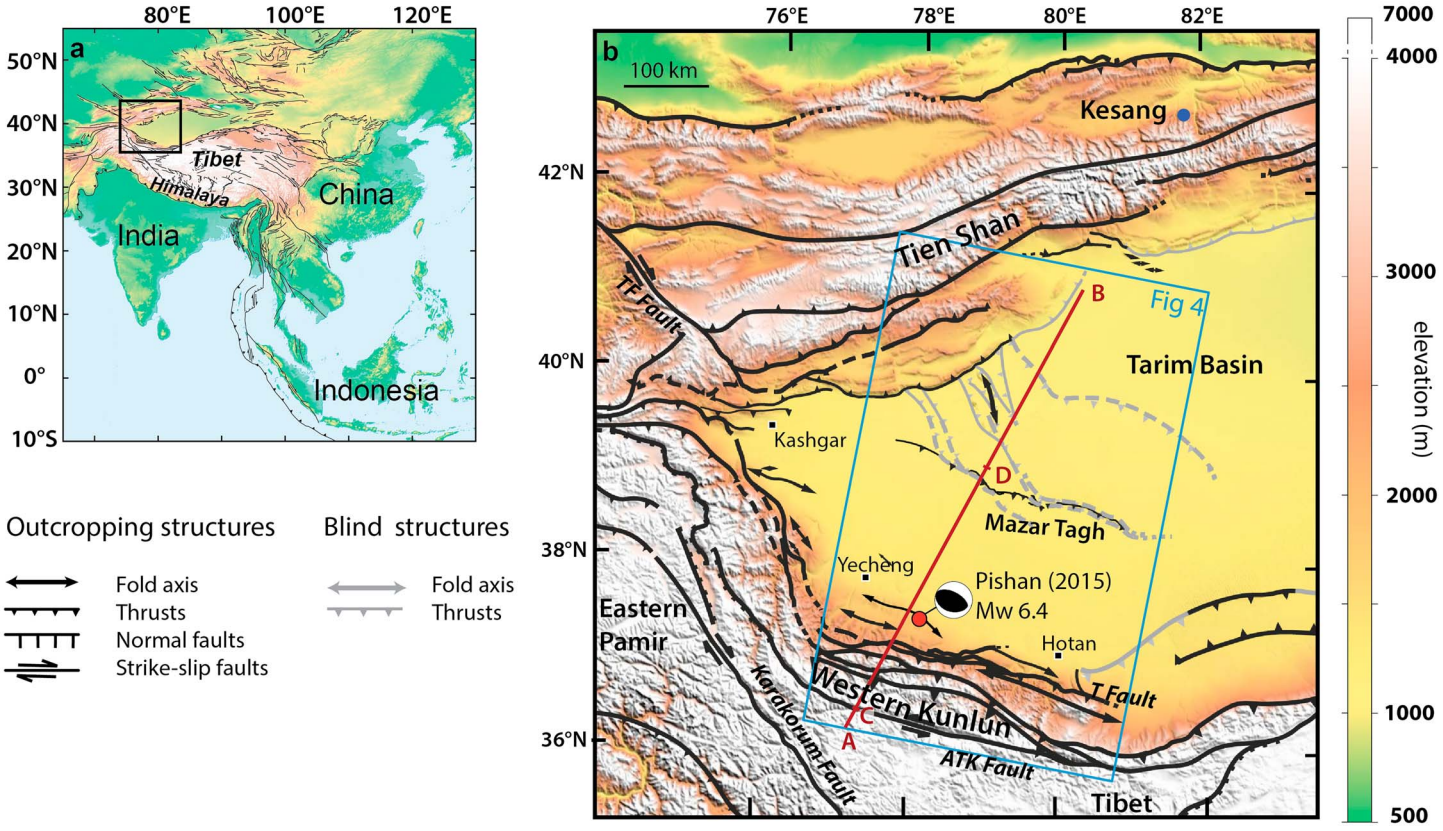


**Figure 1.** Digital topography and major structural features of (a) Asia and (b) West Kunlun area (location indicated by rectangle in Figure 1a). Elevation data are from the SRTM30 digital elevation model and the structural framework from Laborde (2017). Structures are reported in solid or dashed lines when active or inactive, respectively. ATK, TF, and T stand for the Altyn Tagh–Karakax, Talas–Ferghana, and Tiekelik faults, respectively. Red line indicates location of projection axis A–B for elevation, seismicity, and GPS data presented in Figure 3. Blue rectangle shows extent of the geological map presented in Figure 4. Axis C–D (within larger axis A–B) corresponds to the geological cross section reported in Figure 6.

et al., 2004), and gravimetric data (e.g., Jiang, Jin, & McNutt, 2004; Lyon Caen & Molnar, 1984) indicate that this mountain range results from the intracontinental underthrusting of the Tarim Block beneath the northwestern Tibetan Plateau. The Western Kunlun is characterized by high altitudes, and erosion of this growing topography over the last ~23 Myr has significantly contributed to the filling of the presently endorheic Tarim foreland basin (Figure 1), with Cenozoic sediment thicknesses of up to ~8–9 km along the topographic mountain front (e.g., D. S. Li et al., 1996; Métivier & Gaudemer, 1997; Wei et al., 2013). Inside this basin, growth strata in sedimentary series probably younger than 10–15 Ma have been observed on seismic profiles above faults and folds of the mountain front (Guan et al., 2013; Jiang & Li, 2014; T. Li et al., 2016; C. Y. Wang et al., 2013; Wei et al., 2013). This clearly indicates that the mountain range was deforming during the late Cenozoic.

Despite geological evidence for recent tectonic deformation, this region remains almost aseismic, except for earthquakes on the Altyn Tagh–Karakax strike-slip fault to the south of the Western Kunlun range and for three earthquakes ($M_w$ 5–6; ISC catalog) along the topographic mountain front: two in the 1950s and the recent $M_w$ 6.4 2015 Pishan earthquake (He et al., 2016; Wen et al., 2016; Figure 2). Moreover, existing GPS stations record little to no deformation (within measurement uncertainties) across the range (Figure 2). However, most of the stations have been installed and their record interpreted with the purpose of constraining the continental-scale present-day deformation over China and Tibet (Gan et al., 2007; Q. Li, You, et al., 2012; Q. Wang et al., 2001; Zhang et al., 2004), or at a more regional scale across the Tien Shan Range just north of the Tarim Basin (Abdrakhmatov, Aldazhanov, & Hager, 1996; Reigber et al., 2001; Zubovich et al., 2010; Figure 2). In their study of seismic moment accumulation and slip deficit throughout China using GPS data within an elastic block model, H. Wang et al. (2011) determined a shortening rate of 3 ± 2 mm/yr across the Western Kunlun range, with the potential for generating $M_w$ 7.1 earthquakes. Such estimates

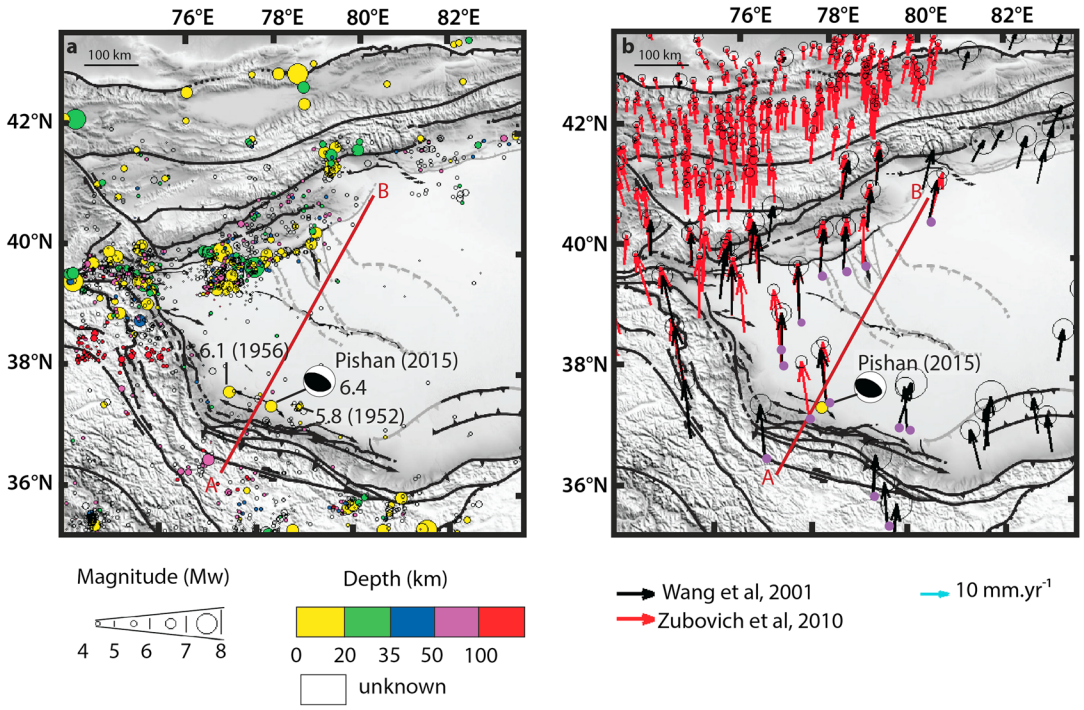


**Figure 2.** (a) Seismicity within our study region (USGC, ISC, recorded from 1904 to 2011). (b) GPS data from Q. Wang et al. (2001; acquired during 10 years) and Zubovich et al. (2010; acquired during 16 years) with respect to stable Eurasia. Error ellipses are 95% confidence intervals for GPS velocities, as determined in the source papers. The red line represents the projection axis A–B reported in Figure 1. Only GPS vectors nearby axis A–B (and reported here with a basal purple circle) were projected in Figure 3.

may however need to be refined with a better account of the actual geometry of potential active structures and to be compared to geological estimates that up to now remain poorly constrained (Avouac et al., 1993; Jiang, Li, & Li, 2013). Finally, because some of the potential active structures root into a decollement of Paleogene evaporites and limestones, the potential for seismic moment accumulation (and subsequent release during major earthquakes) may be questioned, as these lithologies are generally believed to be aseismic. This is particularly critical for seismic hazard assessment given the large dimensions of the corresponding active structures since the most frontal thrust fault emerges at the surface ~150–180 km north of the topographic mountain front, at the Mazar Tagh ridge in the center of the Tarim Basin (J. Pan et al., 2010; Figure 1).

To get further insights into the structural and seismotectonic background of the $M_w$ 6.4 2015 Pishan earthquake and to better quantify the rate of active deformation and the potential for major earthquakes in the Western Kunlun range and Tarim Basin, we hereafter combine a quantitative structural and morphological analysis of the topographic mountain front in the Pishan epicentral area. Based on seismic reflection data, we derive a regional structural cross section in which we identify the fault that broke during the 2015 Pishan earthquake. We combine an analysis of satellite images and DEMs to quantify the incision and tectonic uplift of an alluvial fan and of dated fluvial terraces above this blind fault within the associated Yecheng–Pishan fold. Altogether, we derive the long-term slip rate (over the Pleistocene) on this active structure and discuss our findings in terms of seismic hazards of the region.

## 2. Geological and Climatic Context

### 2.1. Geological Setting

#### 2.1.1. Structure and Stratigraphy of the Western Kunlun Range and Tarim Basin

The Western Kunlun range is a ~700 km long mountain belt located along the northwestern boundary of the Tibetan Plateau, from Kashgar to Hotan (Figure 1). From its overall orientation, this mountain range can be subdivided in two main zones: (1) to the northwest, a north–northwest to south–southeast oriented range from Kashgar to Yecheng, showing an overall structural and stratigraphic continuity with the northeastern

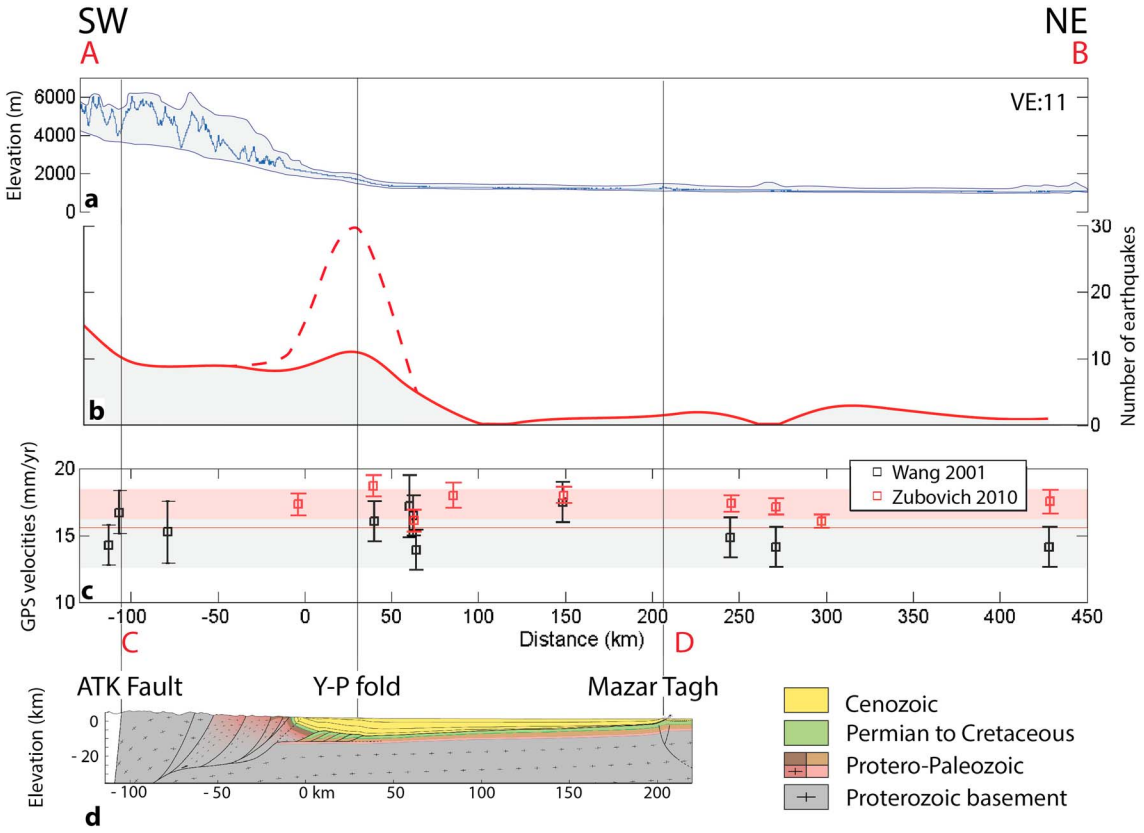


**Figure 3.** (a) Topographic profile. Elevation data are from the SRTM1 digital elevation model, with a vertical exaggeration (VE) of 11. (b) Number of earthquakes (based on ISC, USGS catalogues, as reported in Figure 2) recorded along axis A–B. The dashed envelop corresponds to the contribution of the Pishan event and its aftershocks (from 3 to 25 July 2015) to the total number of earthquakes, as recorded from the same seismicity catalogues. Note that the data on the number of earthquakes was smoothed by cubic interpolation in a 30 km wide window. (c) GPS velocities from Q. Wang et al. (2001) and Zubovich et al. (2010), represented relative to stable Eurasia. Gray and red rectangles represent the average GPS velocities measured north of the Mazar Tagh (see Figure 3d for location), within the reference footwall of the Western Kunlun mountain range, for the data from Q. Wang et al. (2001) and Zubovich et al. (2010), respectively. Elevation, seismicity, and GPS data are projected onto the A–B axis of Figures 1 and 2. Elevation and seismicity are retrieved within a 50 and 100 km wide swath around this projection axis, respectively. (d) Geological cross section shown in detail in Figure 6, given here for structural reference for data in Figures 3a to 3c. ATK: Altyn Tagh–Karakax; Y-P: Yecheng–Pishan.

Pamir; and (2) to the southeast, an east–west oriented range from Yecheng to Hotan, where our study area is located. This latter southeastern part of the range has a length of ~350 km and a width of ~130 km that increases up to ~300–400 km if extended to the Mazar Tagh deformation front far north of the topographic front (Wittlinger et al., 2004). Altitudes rise from ~1200–1300 m in the Tarim foreland to the north, up to ~5500–6400 m at the boundary with the Tibetan Plateau to the south (Figures 1 and 3a).

After a complex Palaeozoic and Mesozoic orogenic history (e.g., Cao et al., 2015; Matte et al., 1996; Mattern & Schneider, 2000; Sobel & Arnaud, 1999), the Western Kunlun range was reactivated during the Cenozoic in response to the India–Asia collision (e.g., Cao et al., 2015; Matte et al., 1996). This range presently corresponds to an orogenic wedge that developed between the Altyn Tagh–Karakax left-lateral fault to the south and the Tarim endorheic foreland basin to the north (Figure 1). This wedge forms above an intracrustal decollement level that progressively shallows from the south to the north. The interior of the mountain range results from the imbrication and exhumation of Protero-Paleozoic basement and Paleozoic cover, whereas the foothills are characterized by a northward-vergent fold-and-thrust belt of Paleozoic, Mesozoic, and Cenozoic sediments (e.g., Guan et al., 2013; Jiang, Li, & Li, 2013; R. Lu et al., 2016; Matte et al., 1996; Wittlinger et al., 2004; Figures 3 and 4). In particular, the topographic mountain front of the Western Kunlun is controlled by a series of folds, such as those located nearby the town of Yecheng and east of it (X. Cheng et al., 2016; Jiang, Li, & Li, 2013; T. Li et al., 2016; R. Lu et al., 2016; Wei et al., 2013). However, the emergent deformation front of the range corresponds to the Mazar Tagh thrust ramp located much further north within the Tarim Basin (e.g., R. Lu et al., 2016; Wittlinger et al., 2004; Figures 1 and 3). To the north, in the footwall of this

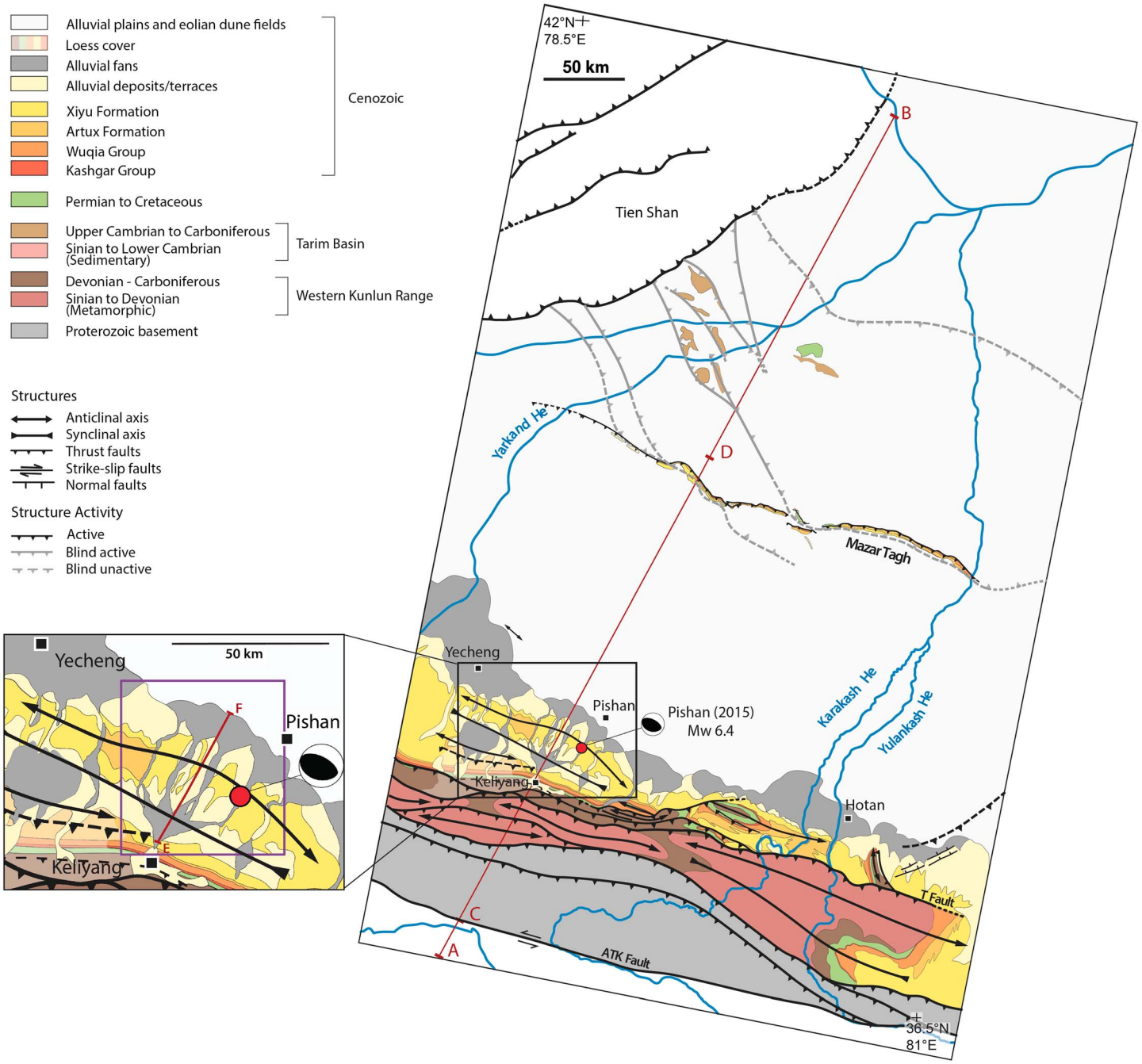


**Figure 4.** Geological map of study area (see blue rectangle in Figure 1 for location) and close-up view on study site of the Yecheng–Pishan fold. Red dot indicates the location of the Pishan earthquake. The red line locates the A–B axis for data projected in Figure 3, the axis C–D locates the geological cross section presented in Figure 6, and axis E–F (in close-up view) the projection axis of the elevation and incision data presented in Figures 8–10. The purple rectangle shows the location of the morphological map of Figure 7. Areas covered by loess are reported with transparency over mapped geological units. Cenozoic formations, from the Xiyu to the Kashgar groups, are defined from their sedimentological facies in the field. ATK and T faults stand for Altyn Tagh–Karakash and Tiekelik faults, respectively.

ramp, large blind Cenozoic structures were also described (Figure 1), but their sealing by Quaternary deposits indicate that they are not currently active (e.g., Tong et al., 2012; C. Wang et al., 2014).

The basement of the Western Kunlun range is composed of Proterozoic to early Paleozoic metamorphic rocks that record deformation associated with the closure of the proto-Tethys during the Ordovician and Silurian (e.g., Matte et al., 1996; Mattern & Schneider, 2000). Within the Tarim Basin, the time-equivalent series have not endured such a metamorphic event and comprise marine calcareous and terrigenous sediments, in

particular with Upper Cambrian gypsiferous shales (Lin et al., 2012; R. Lu et al., 2016; Matte et al., 1996). Below the Western Kunlun foothills, the basal decollement of the range is localized in this Paleozoic evaporitic formation (e.g., R. Lu et al., 2016; C. Y. Wang et al., 2013). Within both the outer mountain belt and the basin, the stratigraphy above basement units is then characterized by a late Paleozoic to Cenozoic, marine to continental, and calcareous to terrigenous sedimentary series (e.g., Lin et al., 2012; R. Lu et al., 2016; Matte et al., 1996). In these series, the Paleocene–Eocene Kashgar Group is composed of gypsum, limestones, and siltstones related to the last marine incursions in the area (e.g., Bosboom et al., 2014; Wei et al., 2013). At the front of the Western Kunlun foothills, in the Tarim Basin, the basal decollement of the range is localized in this latter Cenozoic assemblage (e.g., R. Lu et al., 2016; C. Y. Wang et al., 2013).

Together with these Paleogene deposits, the whole Cenozoic sedimentary sequence can reach thicknesses of up to ~8–9 km within the Tarim Basin along the mountain front near the town of Yecheng. This sequence is related to the erosion of the Tibetan Plateau and of the Western Kunlun/northeastern Pamir mountain ranges to the south (Métivier & Gaudemer, 1997; Wei et al., 2013). Besides the Kashgar Group, this sequence is composed of three prominent lithostratigraphic subdivisions: the continental Wuqia Group, Artux Formation, and Xiyu Formation (Jin et al., 2003; C. Wang et al., 2014; Wei et al., 2013; Zheng, Huang, & Butcher, 2006). The Wuqia Group consists mostly of claystones, siltstones, and sandstones, while the Artux Formation progressively includes conglomerates. The Xiyu Formation is then dominated by conglomerates including some sandy layers. These continental and upward-coarsening sediments can be interpreted as the progressive thrusting of the Tarim Basin by the Western Kunlun range, as has been proposed in other compressive contexts (e.g., Charreau et al., 2009; Dubille & Lavé, 2015; Simoes & Avouac, 2006). It has been clearly demonstrated that the vertical transitions between such lithostratigraphic subdivisions described and defined on the basis of their lithology and facies are not synchronous over foreland basins (e.g., Barberà et al., 2001; Burbank, Raynolds, & Johnson, 1986; Charreau et al., 2009; Heermance et al., 2007). This is also the case for the Wuqia Group, Artux, and Xiyu Formations within our study region (e.g., Heermance et al., 2007; Zheng et al., 2015). Near our study area, along the Kekeya River, a recently revised magnetostratigraphic section indicates an age of ~23 Ma for the base of the Artux formation and a possible age between ~22 and ~15 Ma for that of the Xiyu Formation (Zheng et al., 2015).

The contemporaneous exhumation of the inner Western Kunlun range and propagation of the outer fold-and-thrust belt are thought to have initiated by ~23 Ma, based on thermochronological data (Li et al., 2007; E. Wang, 2003), together with growth strata (X. Cheng et al., 2016; Jiang, Li, & Li, 2013) and increasing sedimentation rates in the southwestern Tarim Basin (Jiang & Li, 2014; Métivier & Gaudemer, 1997). Published estimates on crustal shortening across the Western Kunlun vary from 25–54 km (Jiang, Li, & Li, 2013) to ~80 km (Lyon Caen & Molnar, 1984).

#### 2.1.2. Structure and General Morphology of the Yecheng–Pishan Fold

The folds of the topographic mountain front are appropriate targets to quantify the slip rate on the basal decollement of the Western Kunlun range. Because of abundant incised alluvial fans and fluvial terraces that act as geomorphic markers of deformation, we investigate here the Yecheng–Pishan fold located nearby the epicenter of the 2015 Pishan earthquake (Figure 4). There is no fixed nomenclature in the literature for the name of this particular fold that has been alternatively named the Guman, Piyaman, or Slik fold (e.g., Guan et al., 2013; T. Li et al., 2016; Wei et al., 2013). In this study, we choose for simplicity to name this structure after the two towns located at its lateral extremities.

The Yecheng–Pishan fold is oriented WNW–ESE and extends over a distance of ~140 km along the topographic front of the Western Kunlun range, with a width increasing westward from ~10–20 to ~40 km (Figure 4). Based on existing geological maps and field observations, together with seismic profiles, several cross sections have already been proposed through the topographic mountain front in general (e.g., Jiang, Li, & Li, 2013; Matte et al., 1996; C. Wang et al., 2014; Wang, Cheng, Chen, Li, et al., 2016) and through the Yecheng–Pishan fold in particular (e.g., Guan et al., 2013; T. Li et al., 2016; R. Lu et al., 2016; Wei et al., 2013). In these cross sections, this fold is interpreted as related to a duplex structure at the rear of a frontal blind thrust ramp connecting a deep decollement within Cambrian gypsiferous shales to a shallower one within the Paleogene shallow marine series of the Kashgar Group.

At the surface, the morphological expression of the Yecheng–Pishan fold corresponds to a smooth topographic step, several hundred meters above the present-day sedimentation level of the Tarim Basin

(Figure 3a). Rivers flowing out of the mountain range cross this step through incised valleys perpendicular to the fold axis (Figure 4). Along these valleys, preserved terraces have recorded deformation related to slip on the underlying blind faults.

#### 2.1.3. Seismicity, GPS Displacements, and the 3 July 2015 ($M_w$ 6.4) Pishan Earthquake

Over the short-term (i.e. over ~1 yr to ~10s yrs), the deformation recorded by historical seismicity in the Western Kunlun area seems to be structurally controlled. Indeed, most of the earthquakes are recorded within the mountain range and most specifically along the topographic mountain front if we exclude those associated to the Altyn Tagh–Karakax strike-slip fault to the south (Figures 2 and 3). The frontal thrust sheet, emerging at the Mazar Tagh within the Tarim Basin, shows little to no seismicity. Available GPS data, reported relative to stable Eurasia, do not show any significant gradient across the mountain belt (Figures 2 and 3), although the GPS displacements measured by Zubovich et al. (2010) and Q. Wang et al. (2001) to the south within the range interior appear systematically higher than those measured north of the Mazar Tagh. This is particularly true if the two GPS data sets are considered separately (Figure 3c). However, this tendency is to be verified given the few GPS data and their large uncertainties. If correct, present-day shortening rates across the Western Kunlun would be ~5 mm/yr at most, with a possible decrease in surface displacements across the foothills where the seismicity rate is the highest and where the 3 July 2015 Pishan earthquake occurred (Figures 2 and 3).

The 3 July 2015 Pishan earthquake epicenter is located just below the Yecheng–Pishan fold (Figures 1–3). Different global solutions (USGS, CMT, and GEOSCOPE) agree on a thrust-fault focal mechanism, with nodal planes overall oriented parallel to the mountain range and dipping either ~60° to the north or ~25–30° to the south. The hypocentral depth seems less well resolved, with values mostly of 19–20 km (GEOSCOPE and USGS), but as shallow as 10–15 km for some of the proposed solutions (USGS, CMT), in agreement with some local solutions (T. Li et al., 2016). Refined source parameters of this earthquake have been obtained from the inversion of surface coseismic deformation measurements by InSAR (He et al., 2016; Wen et al., 2016). These inversions suggest that the earthquake ruptured a 24–27°S dipping blind ramp, with coseismic slip concentrated at a shallow depth of 8–16 km.

### 2.2. Climatic Evolution Within the Tarim Basin Over the Quaternary

Aridification of Central Asia and in particular northwest China has occurred over the Cenozoic, with the closure of the Paratethys Ocean and the progressive growth of the Tibetan Plateau (e.g., Bosboom et al., 2014; Fluteau, Ramstein, & Besse, 1999; Ramstein et al., 1997). The climate in this region is presently continental and dominated by the Westerlies and the Siberian high-pressure system because it is isolated from the Asian Monsoon by the Himalayas and Tibet to the south (Aizen et al., 2006). The climate within the Tarim Basin and Western Kunlun range is therefore arid (the Taklamakan Desert, one of the largest sand deserts, stands within the Tarim Basin), with annual precipitations ranging from 30 to ~100 mm/yr and generally less than 50 mm/yr (D. Zheng, 1999; Zhu et al., 1980). However, several paleoclimatic records show significant climatic fluctuations in this region over the Quaternary. In particular, stalagmites from the Kesang Cave (eastern Tien Shan—Figure 1) have recorded variable moisture content in the area over the last 500 kyr (H. Cheng et al., 2012; Figure 5). This stalagmite record is incomplete, with several hiatuses interpreted as representative of arid periods because stalagmites need moisture to grow. Because the periods of stalagmite growth are correlated with times of high Northern Hemisphere summer insolation (Berger, 1978), it has been proposed that the higher regional moisture periods could be due to possible incursions of moisture from the Asian summer monsoon in the region (H. Cheng et al., 2012). According to this interpretation, the climate of the region would have been wetter essentially during interglacial periods, following overall the ~100 kyr Milankovitch cycles, in addition to other minor wetter periods such as by ~40–50 ka and from late Pleistocene to mid-Holocene (~4–13 ka; H. Cheng et al., 2012; Railsback et al., 2015; Figure 5).

Over the late Pleistocene and Holocene, climatic fluctuations between an arid and a relatively more humid climate have been also inferred from the presence of dated lake deposits within the Tarim Basin and fluvial terraces along the Keryia River, to the east of the Western Kunlun termination (Yang et al., 2002, 2011; Yang, Preusser, & Radtke, 2006; Yang & Scuderi, 2010). In particular, extensive lake deposits dated to ~30–45 ka (Yang, Preusser, & Radtke, 2006) correlate well with a possible wetter period by ~40–50 ka from the stalagmite record of the Kesang Cave (H. Cheng et al., 2012; Figure 5). Pond deposits in the lower reaches of the Keryia River have been dated to ~20 ka and ~13 ka, suggesting a wetter climate by this time. In addition,

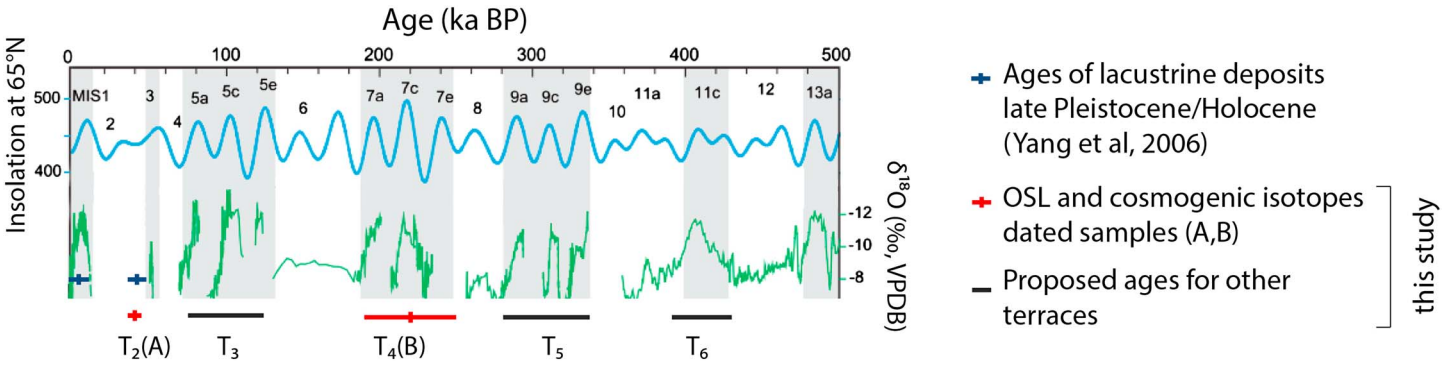


**Figure 5.** Existing paleoclimatic constraints for our study region (modified from H. Cheng et al., 2012), compared to ages of the Yecheng–Pishan terraces. The blue curve indicates summer insolation over the Northern Hemisphere at 65°N (Berger, 1978). Numbers at the top indicate corresponding marine isotopic stages (MIS). The green curve corresponds to the incomplete $\delta^{18}O$ record from the Kesang Cave (H. Cheng et al., 2012; location in Figure 1). Dark blue points report the ages of dated lacustrine deposits within the Tarim Basin (Yang, Preusser, & Radtke, 2006). Red points indicate the ages for terraces T2 and T4 dated by OSL and by in situ produced cosmogenic isotopes (this study). Black segments show proposed ages for terraces T3, T5, and T6 assuming that they are correlated with periods of wetter regional climate similarly to T2 and T4 (see text for further details).

several levels of fluvial terraces dated from ~2 ka to ~6 ka were also interpreted as representative of wetter periods (Yang et al., 2002, 2006, 2011; Yang & Scuderi, 2010). The stalagmite record within the Kesang Cave is complete over the Holocene, suggesting that moisture was sufficient for stalagmite growth.

## 3. Structure of the Yecheng–Pishan Fold

We first construct a geological map and a balanced geological cross section over our study region (Figures 4 and 6). This geological cross section is projected onto a N29° axis, perpendicular to the overall direction of geological structures and perpendicular to the Yecheng–Pishan fold axis. The reference for horizontal distances along our section is chosen as the location of the northernmost subvertical strata nearby the Keliyang River divergence, south of the fold (for location, see point E in Figure 4). In our study area, the fold has a width of ~25 km.

### 3.1. Data and Methods

Based on a combination of existing cartographic documents (e.g., Jiang & Li, 2014; Matte et al., 1996; C. Wang et al., 2014), field observations along river sections crossing the topographic mountain front, and interpretations from satellite images (Landsat and SPOT, as well as DigitalGlobe images available in the Google Earth and Bing databases), we first construct a geological map of the eastern part of the Western Kunlun range and its foreland (Figure 4). On this document, the Cenozoic sediments are mapped according to diachronous lithostratigraphic subdivisions (Kashgar Group, Wuqia Group, Artux, and Xiyu Formations) rather than to particular stratigraphic periods. Indeed, age constraints for these deposits are still scarce and often equivocal within the study area (Sun, 2006; Zheng et al., 2000, 2015), whereas the lithostratigraphic subdivisions can be easily identified in the field on the basis of their facies, or on the basis of their overall color on satellite images.

Thanks to the Sinopec Group of the China Petrochemical Corporation, we also had access to a proprietary seismic reflection profile crossing the Yecheng–Pishan fold within the epicentral area of the 2015 Pishan earthquake and extending from the Western Kunlun topographic front to the center of the Tarim Basin (section C–D in Figure 4). Due to the proprietary nature of the seismic data, this profile cannot be directly shown here, and we only report our interpretation. We follow several key horizons identified from wells and outcrops and performed a time–depth conversion to build the balanced geological cross section presented in Figure 6. Selected key horizons correspond to the bases of the Sinian, Upper Cambrian, Permian, and Cenozoic sedimentary series. Within the Cenozoic sediments, we follow three horizons corresponding to the base of the Oligocene, middle Miocene, and Plio-Quaternary deposits according to the nearby revised magnetostratigraphic ages (Zheng et al., 2015). In these deposits, growth strata are also identified from variations in upsection dip angles and in their lateral thickness. A time–depth conversion of the seismic profile is performed using seismic velocities (supporting information Table S1) derived from well

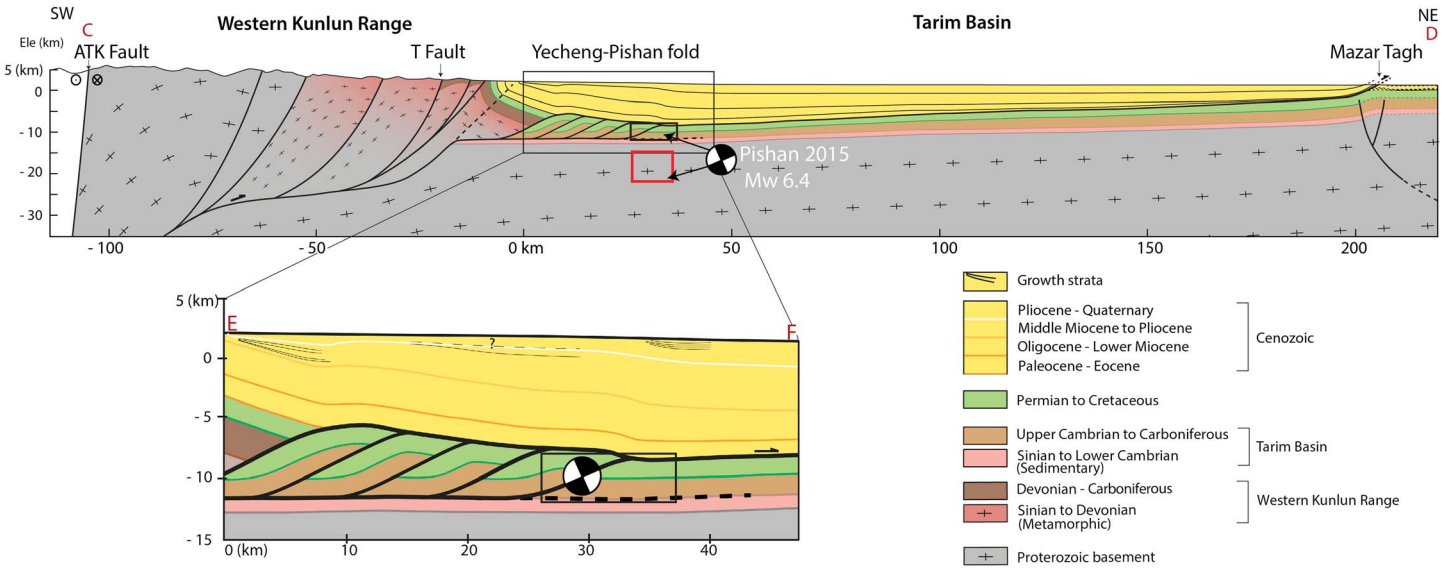


**Figure 6.** Geological cross section along axis C–D derived from field constraints, satellite images, and seismic profiles. ATK and T faults stand for Altyn Tagh–Karakash and Tiekelik faults, respectively. Close-up view on the Yecheng–Pishan fold structural geometry. The reference for horizontal distances is point E of axis E–F (Figure 4), which structurally corresponds to the northernmost subvertical Cenozoic stratum at the Keliyang River outlet along the mountain front (see Figure 4 for location). Cenozoic strata are here not differentiated from their sedimentological facies as within the geological map of Figure 4 and are only reported in yellow. Their chronology is here defined according to seismic profiles and well data, in particular within the close-up view of the Yecheng–Pishan fold in Figure 6. Bold rectangles by the Yecheng–Pishan fold show the possible locations and depths of the $M_w$ 6.4 Pishan earthquake, from the various geodetic (He et al., 2016; Wen et al., 2016) or global solutions (USGS, CMT, and CEA) in black and red, respectively. For consistency with structural constraints, the focal mechanism is projected on the Yecheng–Pishan blind ramp, within the close-up view of Figure 6.

data (Laborde, 2017). We then combine the depth-converted interpretation of this profile with our geological map to build the balanced geological cross section (Figure 6). In this cross section, it should be noted that the Cenozoic subdivisions follow the seismic horizons described above and not the lithostratigraphic units represented on the geological map (Figure 4). Because the lithostratigraphic units are diachronous, there is no clear and simple correlation between their boundaries and the isochronous seismic horizons of our cross section.

### 3.2. Geological Cross Section

#### 3.2.1. General Results and Observations

Figures 4 and 6 show the obtained geological map and cross section. They document the structure of the Western Kunlun thrust wedge between the Altyn Tagh strike-slip fault to the south and the Mazar Tagh thrust ramp to the north. To the south, in the range interior, imbricates of metamorphic basement are thrusted northward along the Tiekelik Fault, over imbricates of metamorphic basement and Paleozoic sedimentary cover. The detailed structure of this inner part of the range is poorly constrained due to limited access, but connecting the major faults within the metamorphic basement to a crustal ramp and basal decollement beneath the range seems a reasonable hypothesis, as previously proposed by Matte et al. (1996) and Wittlinger et al. (2004). In front of these imbricates, steep (up to vertical) Paleozoic to Cenozoic strata sharply give rise to flatter deposits through the hinge of an asymmetric syncline.

To the north of this syncline, within the foothills, the Yecheng–Pishan fold deforms the Paleozoic to Cenozoic sedimentary cover of the Tarim Basin and localizes the topographic mountain front (Figures 4 and 6). In this outer part of the system, the seismic profile provides clear evidence for an upper-crustal foreland-vergent duplex structure at the rear of a blind thrust ramp. This ramp connects the deep decollement within Cambrian gypsiferous shales to the shallower one within the Paleogene evaporitic and shallow marine series (Figure 6).

No particular structure or deformation pattern is observed further north within the southern Tarim Basin, except for the Mazar Tagh fold and thrust (Figure 6). Field, satellite, and seismic observations clearly indicate that the Mazar Tagh thrust has a northward vergence similar to that of the Western Kunlun and that it roots

into the Paleogene shallow marine and evaporitic series. Basement structures beneath the Mazar Tagh can be observed in seismic profiles, and these have led to some confusion in previous structural interpretations (e.g., T. Li et al., 2016; C. Wang et al., 2014; Wittlinger et al., 2004), but their sealing by recent Quaternary deposits indicates that they are currently no longer active (e.g., Tong et al., 2012; C. Wang et al., 2014). In any case, we are not able to propose a kinematically viable solution to transfer slip from these basement faults onto the Mazar Tagh thrust ramp.

#### 3.2.2. Structure of the Yecheng–Pishan Fold

From the seismic profile and relying on the hypothesis of conservation of areas during the deformation process to keep a balanced cross section, we interpret the deep structure of the Yecheng–Pishan fold as a duplex with a stack of four thrust slices between the deep Cambrian decollement and the shallow Paleogene one (Figure 6). At the front of this duplex, the blind ramp that connects these two decollements is found at a depth of 12 to 8 km, with a dip angle of ~25°. From this geometry, we derive a total cumulative shortening of 14 to 15 km across the whole duplex. The presence of the hindmost thrust sheet is debatable since it is located in a zone of poor seismic imaging. In the case that this sheet is nonexistent, a minimum total shortening of 9 to 10 km is derived. In any case, 1.5 to 2.5 km of shortening is accommodated across the sole most frontal thrust slice. Our structural interpretation is rather simple, with one single surface anticline, and we do not find any particular evidence for additional complexities from our seismic profile nor from published structural measurements (T. Li et al., 2016), as has been proposed in previous studies (T. Li et al., 2016).

Growth strata derived from the seismic profile indicate that deformation initiated during the upper Miocene across the overall duplex and during the Plio-Quaternary on its frontal thrust ramp (Figure 6). The kinematics of deformation across the Yecheng–Pishan fold therefore follows a classical forward-breaking sequence. More precise age estimates can be proposed for growth strata and folding inception by assuming constant sedimentation rates derived from sediment thicknesses and from the age of the seismic horizons. From the ~2–3 km thick middle–upper Miocene series at the top of the fold, we derive a sedimentation rate of ~0.2–0.3 mm/yr. Similarly, a sedimentation rate of ~0.4 mm/yr is found from the ~2 km thick Plio-Quaternary deposits at the front of the fold. By assuming these sedimentation rates as constant over these periods of time, the age of observed growth strata indicate that deformation initiated by ~5.5 to ~7 Ma across the overall duplex and by ~2 to ~3 Ma on its frontal thrust ramp. These values and the total shortening imply a long-term shortening rate of 2 to 2.6 mm/yr across the whole structure and of 0.8 to 1.1 mm/yr on the frontal thrust only. Using the minimum amount of total shortening derived previously, our minimum long-term shortening rate across the whole structure would be 1.4 to 1.8 mm/yr.

It can be noticed that growth strata are also visible within the syncline to the south of the Yecheng–Pishan fold (Figure 6). These growth strata indicate a middle to upper Miocene period of tectonic activity for the associated structure further south, that is, before deformation initiated on the Yecheng–Pishan duplex.

Finally, given the location, depth, and focal mechanism of the Pishan earthquake, together with our data on the geological and structural background of the region, we follow previous authors (T. Li et al., 2016; R. Lu et al., 2016) on the idea that the Pishan earthquake ruptured the south-dipping blind ramp at the front of the Yecheng–Pishan duplex. We therefore favor the shallower hypocentral depths (black frame in Figure 6) proposed in some of the global (USGS and CMT) or local (T. Li et al., 2016) solutions.

#### 3.2.3. Regional Cross Section

The blind ramp beneath the Yecheng–Pishan fold transfers slip from the Cambrian deep decollement into the Paleogene shallow one. Slip then needs to be transferred upward to the surface, either backward passively onto the Paleogene decollement as in the case of passive-roof backthrusts observed in some foreland basins (e.g., Bonini, 2001) or forward into the Tarim Basin. The former case is not consistent with the observed absence of growth strata concomitant to duplexing beneath the Yecheng–Pishan fold (i.e., upper Miocene to present) within the syncline south of the fold, where the Paleogene series is exhumed (Figure 6). Alternatively, we therefore favor the idea that slip is transferred forward into the Tarim basin. The absence of deformation within the Cenozoic strata of the southern Tarim Basin and the simple observation that the Mazar Tagh thrust roots into the same Paleogene series and that it has a northward vergence imply that the shallow Paleogene decollement extends northward from the Yecheng–Pishan fold into the southern half of the Tarim Basin and reaches the surface at the Mazar Tagh thrust ramp (Figure 6).

The emergent deformation front therefore lies ~150–180 km north of the topographic mountain front, with a large frontal thrust sheet showing no internal deformation. Such peculiar structure could be related to the low long-term friction of the Paleogene decollement containing some evaporites or be favored by the extreme sedimentation along the mountain front as suggested by some analog experiments on the interactions between tectonics and sedimentation (e.g., Bonnet, Malavieille, & Mosar, 2007; Fillon, Huismans, & Van Der Beek, 2012; Mugnier et al., 1997; C. Y. Wang et al., 2013). The proposed cross section thus implies simple kinematics with a major basal detachment shallowing northward beneath the mountain range and southern Tarim Basin. This suggests that the slip transferred into the shallow Paleogene decollement at the front of the Yecheng–Pishan fold is transferred and released over the long-term at the Mazar Tagh thrust ramp. In agreement with R. Lu et al. (2016), Suppe et al. (2015), and Wittlinger et al. (2004), our structural section across the Western Kunlun foothills and the southern Tarim Basin differs from others previously published (T. Li et al., 2016; C. Wang et al., 2014) in the fact that we connect the Mazar Tagh frontal fault to the structures of the topographic mountain front through the Paleogene decollement. As previously detailed, this interpretation is the only one that presently satisfies all structural and kinematic observations.

## 4. Geomorphology of the Yecheng–Pishan Fold Nearby Pishan

To unravel the recent tectonic activity on the blind ramp beneath the Yecheng–Pishan fold, we perform a geomorphological analysis of a site near the epicenter of the 2015 Pishan earthquake and near our structural cross section (for location, see rectangle in Figure 4). At this particular location, the Keliyang River flows out of the Western Kunlun mountain range and diverges into four channels (labeled R1 to R4 from west to east) that cross the Yecheng–Pishan fold (Figure 7). Several terraces have been preserved along these four channels.

### 4.1. Data and Methods

Active alluvial fans and incised fluvial terraces are mapped within our study site (Figure 7) and further analyzed to derive incremental tectonic uplift and shortening since their formation and abandonment (e.g., Lavé & Avouac, 2000). Our mapping is based on a 2.5 m resolution SPOT satellite image of the site, together with satellite images from the Google Earth database. The SPOT image is ortho-rectified using a 20 m resolution SPOT digital elevation model (DEM) of the study site (Figure 7). This DEM is complemented by the use of SRTM1 (30 m resolution) and SRTM3 (90 m resolution) DEMs at a regional scale.

Active alluvial fans are identified from their characteristic fan morphology (i.e., their radial slope pattern). Fluvial terraces are abandoned riverbeds and are identified as relatively planar surfaces delimited by risers. Such morphologies can be clearly identified from satellite imagery and local slope maps derived from the available DEMs. Fluvial terraces of the same age (and therefore corresponding to the same former riverbed) are expected to form an overall continuous surface across and along the present-day river valleys. However, the fluvial terrace record of ancient riverbeds is often discontinuous within a river valley, in particular for the oldest and highly incised remnants. Within each one of the four valleys crossing the Yecheng–Pishan fold within our study site, the different terrace levels are thus defined by locally correlating discontinuous terrace patches using topographic profiles across and along stream. Once the terraces are identified and correlated, terrace elevation data are extracted from available DEMs (in particular the 20 m resolution SPOT DEM) over all their surface to quantify terrace incision.

Some of the mapped terraces were sampled for dating. OSL (optically stimulated luminescence) was used to date one of the lowest terrace levels. A ~50 cm thick sand lens was sampled within fluvial gravels and ~4 m below the top of the terrace (Figure S1-a in the supporting information). The sample was processed at the Nordic Center for Luminescence Dating (Risöe, Denmark). Additional details on the sample processing and analytical characteristics are reported in the supporting information (section S1a; Guérin et al., 2012, 2017; Guérin, Mercier, & Adamiec, 2011; Hansen et al., 2015; Murray, 1996; Murray et al., 1987, 2012; Murray & Wintle, 2000, 2003; Prescott & Hutton, 1994; Thomsen et al., 2016). Three higher surfaces were sampled for dating using in situ produced cosmogenic isotopes ($^{10}$Be and $^{26}$Al). All samples were prepared at the cosmogenic isotope laboratory of the University of Strasbourg (Strasbourg, France), and accelerator mass spectrometry measurements were performed with the ASTER spectrometer at the CEREGE (Aix-en-Provence, France). A depth profile, from the surface down to a depth of 5–6 m, was collected along a terrace riser for the lowest of these three surfaces (Figure S1-b5 in the supporting information). An amalgam of samples was considered for the surface production of $^{10}$Be and $^{26}$Al. At various depths, single cobbles with dimensions of 5–15 cm

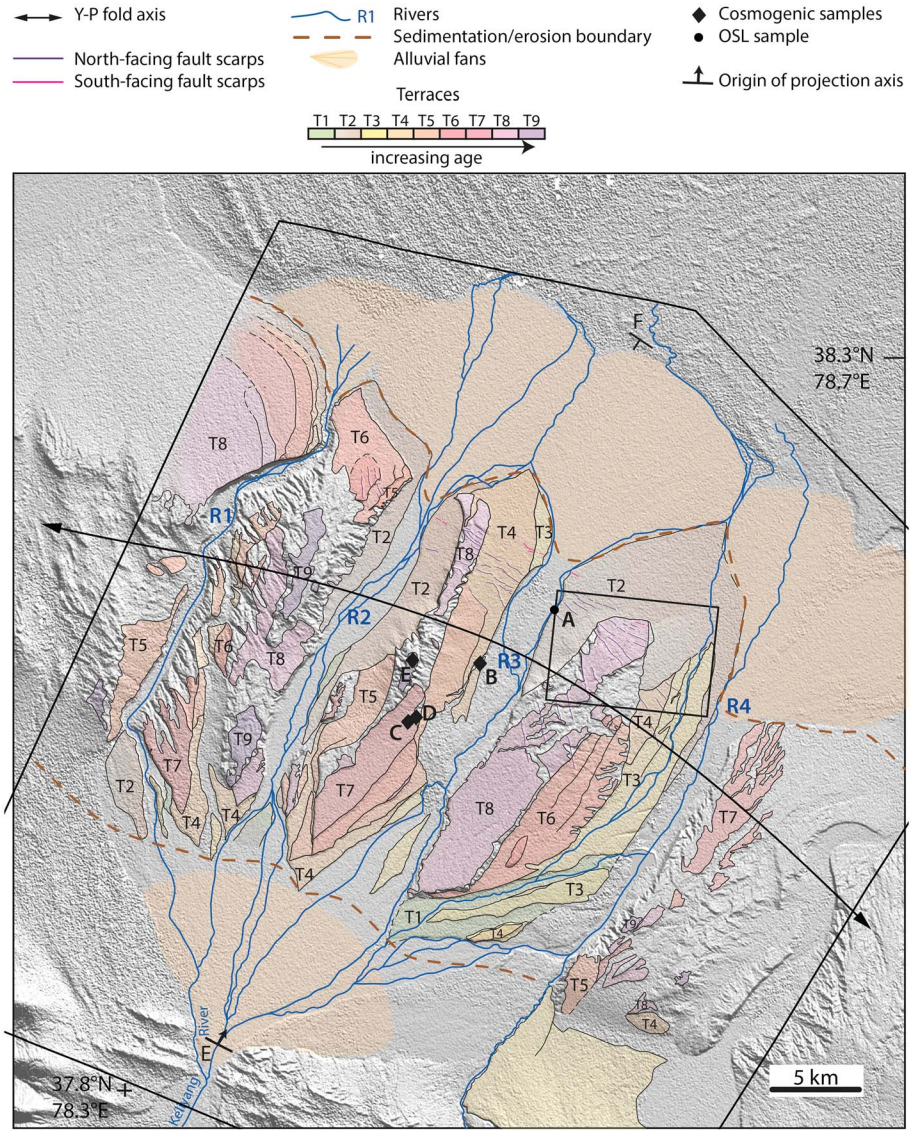


**Figure 7.** Morphological map of the terraces of the Yecheng–Pishan fold at our study site. Elevation data are from SRTM1 and SPOT DEMs. Black frame corresponds to the spatial extent of the SPOT image and mapping. Dated samples are represented by black diamonds and dots and noted A to E from youngest to oldest ages. Rivers crossing the fold are labeled R1 to R4 from west to east, respectively. Point E noted with an arrow corresponds to the reference for horizontal distances along the profiles of Figures 3, 6, and 8–10. The black rectangle shows the location of Figure S2-b.

were collected. In the case of the two higher surfaces, amalgamated samples were collected at the surface and at a depth of 30–40 cm. Additional details on the sample processing and analytical characteristics are reported in the supporting information (section S1-b; Balco et al., 2008; Brown et al., 1991; Gosse & Phillips, 2001; Kohl & Nishiizumi, 1992; Lal, 1991; Stone, 2000). Ages are synthesized in Table 1 (see supporting information for additional details).

### 4.2. Geomorphological Map of the Yecheng–Pishan Fold

Figure 7 illustrates the morphological map of our study site within the Yecheng–Pishan fold. A first-order observation from our mapping is that the morphology of this site obeys a particular organization in three major zones along stream and across strike. First, nearby the oasis of Keliyang and to the south of the fold, the Keliyang River flows out of the mountain range (where it drains a surface of ~2710 km$^2$—Figure S2-a in the supporting information) into a relatively flat area where it splits into four channels. Incision of these channels is limited in this area, and sedimentation prevails. This area shows the characteristic morphology of an alluvial fan (Figures 7 and S2-a). Then, farther north and downstream, these four channels cross the

**Table 1**
*Ages Obtained or Attributed for the Terraces Mapped Within the Yecheng–Pishan Fold*

| Terrace level | Age (ka) | Dating method (sample) |
|---|---|---|
| T2 | 40 ± 3 | OSL (A) |
| T3 | 80–120 | Estimated |
| T4 | 220 ± 30 | Cosmogenic isotopes (B) |
| T5 | 285–335 | Estimated |
| T6 | 390–430 | Estimated |
| T7 | >1,500 | Cosmogenic isotopes (C and D) |
| T9 | >1,500 | Cosmogenic isotopes (E) |

*Note.* In the case of actually dated terraces, ages are either obtained from OSL (optically stimulated luminescence) or using in situ produced cosmogenic isotope $^{10}$Be (see supporting information for further details). Other terrace ages are estimated by comparison to regional paleoclimatic data (Figure 5). Samples are reported from A to E and localized on the map (Figure 7) and the elevation profiles (Figures 8 and 9)

Yecheng–Pishan fold within narrow valleys characterized by a higher topographic relief and the presence of incised and uplifted fluvial terraces. This area is dominated by river incision. Finally, farther north, the four channels flow into the Tarim Basin forming alluvial fans of similar sizes at their respective outlets (Figure 7). Because the sedimentation–incision–sedimentation pattern across the Yecheng–Pishan fold is correlated to the geometry of the structure at depth (Figure 8), we propose that active tectonics exerts a first-order control on the morphology of our study site.

The drainage organization of this site is at odds with the usual stream hierarchy in which channels branch together and converge downstream (Figures 7 and S8). Moreover, across the fold, the altitudes of the two outer channels R1 and R4 are systematically lower (by up to ~50 m) than those of the two inner channels R2 and R3 when projected perpendicular to the fold axis. Such pattern, with a downstream diverging flow, is usually observed for alluvial fans. Indeed, the ~50 m difference in altitude is comparable to the variation in altitude observed laterally between the center and the sides of the active fans south and north of the Yecheng–Pishan fold (Figure 8), implying average lateral slopes of 0.1–0.2° given the dimensions of the fans. We therefore assume that the four channels crossing and incising into the Yecheng–Pishan fold are the relicts of a former wide alluvial fan that deposited at the outlet of the Keliyang River along the mountain front (Figure S2-a). Incision of the fold by the four through-flowing channels should have

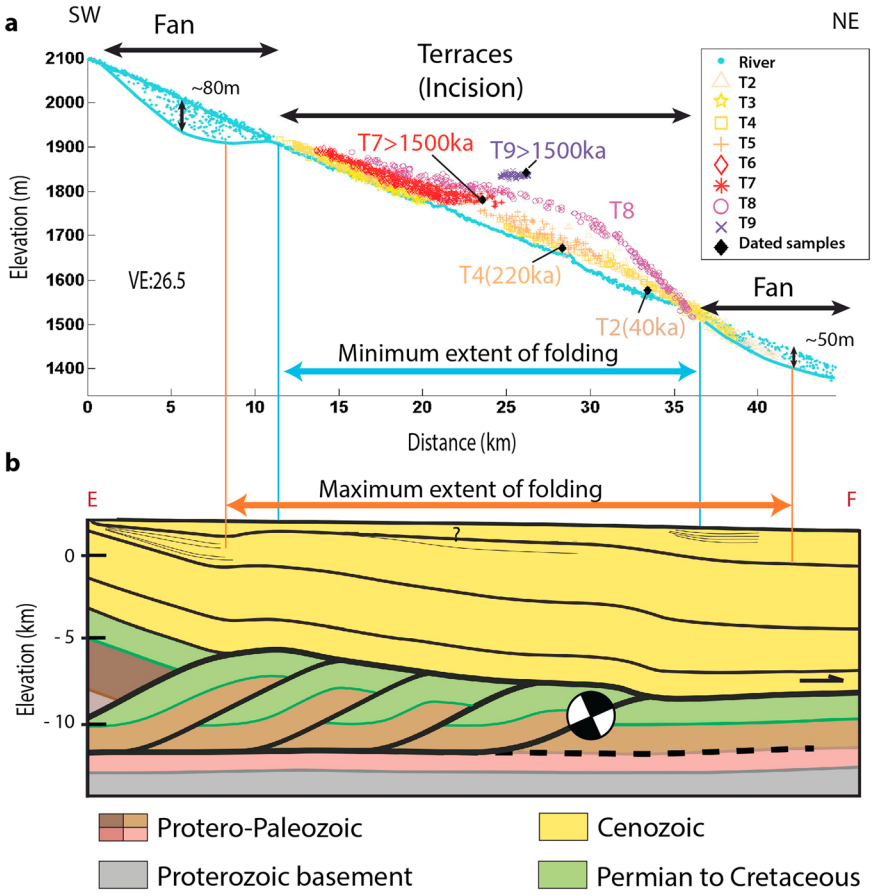


**Figure 8.** (a) Elevation profiles of mapped terraces along channel R3. The locations of the dated samples are reported by black diamonds (see Figure 7 for location in map view). Vertical exaggeration (VE) of 26.5. (b) Geological cross section along axis E–F (see Figure 4 for location and Figure 6 for cross section). The across-strike minimal extent of folding is derived from the lateral extent of river incision, whereas the maximal extent of folding corresponds to the maximal folding extension as observed within the seismic profile.

occurred subsequently to this initial fan deposition and accompanied the morphological expression of the fold. The overall fan morphology has been maintained despite subsequent tectonic deformation on the Yecheng–Pishan blind ramp (Figure S2-a). According to this interpretation, the topmost morphological surfaces preserved within our study site may thus correspond to the depositional surface of an initial alluvial fan, rather than to fluvial terraces sensu stricto.

Along the four rivers incising across the fold (R1 to R4 from west to east), we map up to nine levels of distinct preserved surfaces (labeled T1 to T9 from the lowest and youngest terrace to the uppermost and oldest one; Figure 7). The topmost surface (T9) is found along the drainage divide between adjacent valleys and is interpreted as the depositional surface of a former single and wide alluvial fan. Lower surfaces are interpreted to be fluvial terraces representative of the incision regime that followed abandonment of the former alluvial fan surface.

Not all nine surface levels are found within the different valleys, but at least eight levels are preserved in each one, some very partially (T1 and T9). Within each valley, most levels are only well preserved on one river bank (either the eastern or the western river bank). Therefore, we first label the relative stratigraphic position of each terrace level separately within the four valleys crossing the fold. Then, we cross correlate the terrace levels all over our study site based on those common to two adjacent valleys. This is the case for terrace levels found along the drainage divide separating two adjacent rivers along the fold crest (mostly T9, T8, and T7), but also at the transition from sedimentation to incision—and vice versa—along the two fold limbs. As we find an identical relative stratigraphic position of each terrace level from one valley to the other, we finally use a common labeling from T1 up to T9 all over our study site (Figure 7).

Furthermore, our morphological mapping highlights the presence of numerous fault scarps along the northern limb of the Yecheng–Pishan fold over most of our study site (Figure 7 and Figure S2-b in the supporting information), as already noticed by T. Li et al., (2016). These faults are normal faults and small-scale structures and are not visible on the studied seismic profile. We interpret these secondary faults as accommodating folding above a thrust with a variable geometry at depth, in particular at the transition from the thrust ramp to the fault flat of the Paleogene decollement along the northern part of the Yecheng–Pishan fold (Figure 6). Because they accommodate folding and because their incremental scarps are rather minor at the scale of the whole fold, these faults do not have any particular impact on our subsequent analysis. Further details on these structures are reported in the supporting information S2.

### 4.3. Age Constraints on Fluvial Terraces: Implications for the Climatic Origin of Terraces

Four surfaces within the valley of channel R3 have been sampled for dating (Figure 7). OSL was used to date deposition of terrace T2. T4, T7, and T9 were sampled for dating their surface abandonment by using in situ produced cosmogenic isotopes ($^{10}$Be).

Our results indicate that the two highest sampled surfaces T7 and T9 are old enough to have reached secular equilibrium in which $^{10}$Be production and radioactive decay balance each other. Given this and the few collected samples, we can only propose indicative minimum ages of 1.5 Ma for both of these surfaces (Table 1 and supporting information). In contrast, the OSL and in situ produced cosmogenic $^{10}$Be analyses indicate well-constrained ages of 40 ± 3 ka and 220 ± 30 ka for the two other terraces T2 and T4, respectively (supporting information, Table S2). The age of 220 ± 30 ka for T4 is obtained in the absence of surface erosion. Considering the erosion rate deduced from the older terraces, we get an age of 250 ± 35 ka for T4 (supporting information S1).

Fluvial terraces are usually interpreted as associated to higher river discharges and/or higher sediment fluxes related to regional climatic variations (e.g., Bull, 1991; Burbank & Anderson, 2011), but these geomorphic markers may also be related to the evolution of the upstream drainage basin (e.g., Simoes, Chen, & Shinde, 2014) or be autogenic (e.g., Finnegan & Dietrich, 2011) independently of climate or tectonic changes. In the case of the site investigated here, ages of 40 ± 3 ka and 220 ± 30 ka for terraces T2 and T4 in channel R3 are well correlated with two of the regional wetter climatic periods proposed from the paleoclimatic record of the Kesang Cave (H. Cheng et al., 2012; Figure 5). In the case of T4, this correlation is clearest for the age of 220 ± 30 ka determined with a no-erosion hypothesis. We therefore favor this age value for this surface and consider that erosion of the flat terrace surfaces is overall negligible within our study area over such periods of time (see supporting information S1b for more details).

If this temporal correlation of terrace formation and abandonment to a wetter regional climate also applies for the other nondated terraces of channel R3, an estimate of their age could be possible from the dated periods of higher moisture content in the region. Indeed, the number of mapped terrace levels, their stratigraphic position, and their relative and absolute ages can be well correlated to the paleoclimatic record of the Kesang Cave, at least for the five lower and younger terrace levels (Figure 5). The relative stratigraphic position of each surface level (from T1 to T9) is identical from one valley to the other, suggesting that the formation of each particular surface level most probably occurred at the same time period all over the study site. We therefore extend our reasoning along channel R3 to over all our study site and interpret the mapped terraces to be of climatic origin. Such an idea of a climatic origin of terraces and fans has already been proposed in the region, within the southern Tarim Basin (Avouac et al., 1993; Yang et al., 2002) or elsewhere farther west and north (Huang et al., 2014; T. Li et al., 2013; H. Lu, Burbank, & Li, 2010; B. Pan et al., 2003; Thompson Jobe et al., 2017).

From the paleoclimatic record of the Kesang cave, we propose probable age intervals for T3, T5, and T6 of 80–120 ka, 285–335 ka, and 390–430 ka, respectively (Figure 5, Table 1), relatively consistent with terrace ages of ~110–130 ka (T. Li et al., 2013), ~350 ka, and ~430 ka (Huang et al., 2014) proposed within the Tien Shan and Pamir Ranges farther north. As the paleoclimatic record does not extend for periods older than 500 ka, further constraints on the ages of T7, T8, and T9 cannot be proposed. In any case, because in situ produced $^{10}$Be ages suggest that these surfaces are at least 1.5 Ma old, there seems to be a large time gap between terraces T1–T6 and surfaces T7–T9.

## 5. Kinematics of Active Shortening From Terrace Morphology and Ages

### 5.1. Approach

Terrace treads are useful geomorphic markers to derive the kinematics of folding and faulting at the timescale of tens to hundreds of kiloyears, that is, over several seismic cycles (Lavé & Avouac, 2000). River incision (i.e., altitude of the terrace tread relative to the present-day active river—Figure 9) can be used to quantify incremental tectonic uplift provided that corrections for changes over time in river sinuosity, gradient, and base level are accounted for (e.g., Lavé & Avouac, 2000). Incremental shortening and slip on the underlying fault can then be quantified from the pattern of tectonic uplift.

A model of deformation can be used in the case that the geometry of the underlying fault and the folding mechanism are well defined. Otherwise, using the principle of mass conservation, the integral of the tectonically uplifted area $A$ of a fold can be directly related to the surface that slid above the basal decollement behind this fold, and it can therefore be used to quantify incremental shortening (Figure 10a; e.g., Lavé & Avouac, 2000):

$$A = d{\cdot}h \tag{1}$$

where $d$ is the incremental shortening and $h$ is the depth of decollement beneath the reference topography (e.g., the river profile). This approach, which is solely based on the hypotheses of mass conservation and deformation by plain strain, is independent of the folding mode and does not require any particular knowledge about it. It only requires knowledge of the depth of the decollement behind the zone of active uplift, in addition to a record of tectonic uplift continuous enough across the study site to properly define the uplifted surface.

### 5.2. Terrace Incision and Incremental Tectonic Uplift

Terrace incision is defined as the altitude difference between the terrace tread and the present-day active channel (Figure 9). We extract the altitude of the terraces from our DEM by considering points covering the whole mapped terrace surfaces, rather than by using local topographic profiles. By doing this, we account for the roughness of the terrace surface, as well as for the uncertainties on the DEM. We measure terrace incision along the long profiles of each channel R1 to R4. Finally, the incision data are projected along a N29° axis perpendicular to the fold axis, for each level from T1 to T9 (see Figure 7 for location).

Overall, the incision pattern for each terrace level across the fold is relatively consistent over all our study site (Figure 9 and Figure S3 in the supporting information), which supports the idea that all remnants of a terrace level have the same age independently of the channels R1 to R4 they were initially associated with. Such a

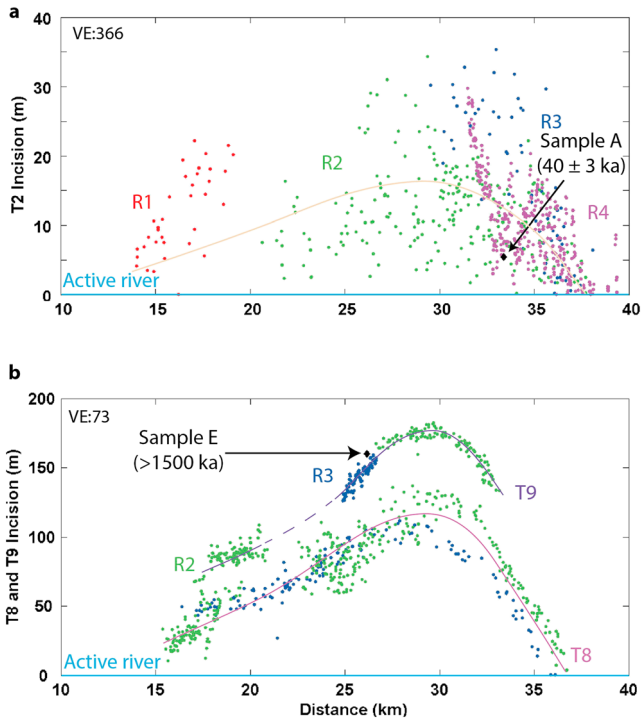


**Figure 9.** (a) Incision profile for terrace T2, by considering T2 terrace remnants over our whole study site (Figure 7). The remnants preserved in the different river valleys are shown in red, green, blue, and magenta for channels R1 to R4, respectively. Dated sample A is reported. (b) Incision profiles for terraces T8 and T9, when considered over the whole study site. The remnants preserved in the different valleys are shown in green and blue for channels R2 and R3, respectively. Sample E is reported. Note the scale difference in the vertical axes of both graphs, with a vertical exaggeration (VE) of 366 and 73 in Figures 9a and 9b, respectively. Continuity in terrace remnants is best visible in the case of older terraces (Figure 9b), because cumulated incision clearly predominates over data scatter.

finding allows for combining the discontinuous terrace record from each single channel into a continuous incision profile for each terrace level across the whole fold (Figures 9 and S3). It should be noted that we do find however some systematic inconsistencies, with incision values lower by up to ~50 m when retrieved from the inner channels R2 and R3 when compared with those retrieved from the outer channels R1 and R4. We already noted the similar altitudinal difference between active channels R2 and R3 relative to R1 and R4. We interpret these systematic inconsistencies to the overall initial fan morphology of our study site (Figure 7). However, this scattering related to lateral variations in incision due to morphological—rather than to tectonic—processes is included in the large uncertainties of our results.

We then consider the composite incision profile of each terrace level taken over the whole study site and apply corrections for changes in river geometry over time to derive incremental tectonic uplift. In each valley R1 to R4, terrace remnants show an elongated pattern parallel to the present-day active channels (Figure 7). From the morphology of the terraces, we therefore do not find any particular evidence for changes in the river sinuosity over time. Moreover, the incision profiles obtained across the fold simply show folding (Figures 8 and 9), with no particular residual baseline slopes that could be interpreted as related to river gradient changes (e.g., Poisson & Avouac, 2004; Simoes, Chen, & Shinde, 2014). From these simple observations, we do not find any evidence for significant river gradient changes during the time span of terrace formation and incision (further details in supporting information S3; Lavé & Avouac, 2000; Milana & Ruzycki, 1999; Milana & Tietze, 2002; Whipple & Tucker, 1999; Yang, Preusser, & Radtke, 2006). For these reasons, we neglect corrections related to changes in river sinuosity and gradient. However, measured river incision needs to be corrected for the base level changes due to sedimentation at the front of the Yecheng–Pishan fold. Having no constraints on the sedimentation rate in this area at the timescale of the uplifted terraces, we use a 0.2 to 0.6 mm/yr sedimentation rate derived from the value of ~0.4 mm/yr deduced from the ~2 km thick Plio-Quaternary deposits just north of the Yecheng–Pishan fold, to which we associate an arbitrarily large 50% uncertainty. Uplift is therefore deduced by correcting terrace incision solely from base level sedimentation. Given the combined incision profiles, the incision rates along the inner channels R2 and R3 are estimated along the fold axis to be ~0.2 mm/yr over the last ~500 kyr, from dated terraces. When compared to the deduced sedimentation rate, it appears that incision only contributes to 25–50% of the uplift rate at most.

On the basis of the uplift pattern determined from the composite incision profiles corrected from sedimentation at the river base level, the incremental uplift recorded by each terrace level is determined (Figure 10 and supporting information S3). The uplifted area *A* (equation (1)) is constrained for each terrace level as the integral of the uplift pattern across the whole fold (Figure 10). To precisely and conservatively retrieve the integral *A* for each uplifted terrace, we define for each terrace level an envelope of minimum and maximum uplift (Figure 10):

1. The minimum uplift pattern is defined from the minimum incision obtained directly from the DEM, corrected by the minimum change in base level. The minimum base level correction is calculated by considering the minimum sedimentation rate of 0.2 mm/yr with the minimum possible age value (Table 1). The minimum uplift is then integrated over the minimum extent of folding, here defined by the horizontal extent of incision across the fold (Figure 8).
2. The maximum uplift pattern across the fold is determined from the maximum incision directly measured from the DEM, corrected using the maximum sedimentation rate of 0.6 mm/yr and by considering the maximum possible age of terraces (Table 1). This uplift pattern is then integrated across the maximum

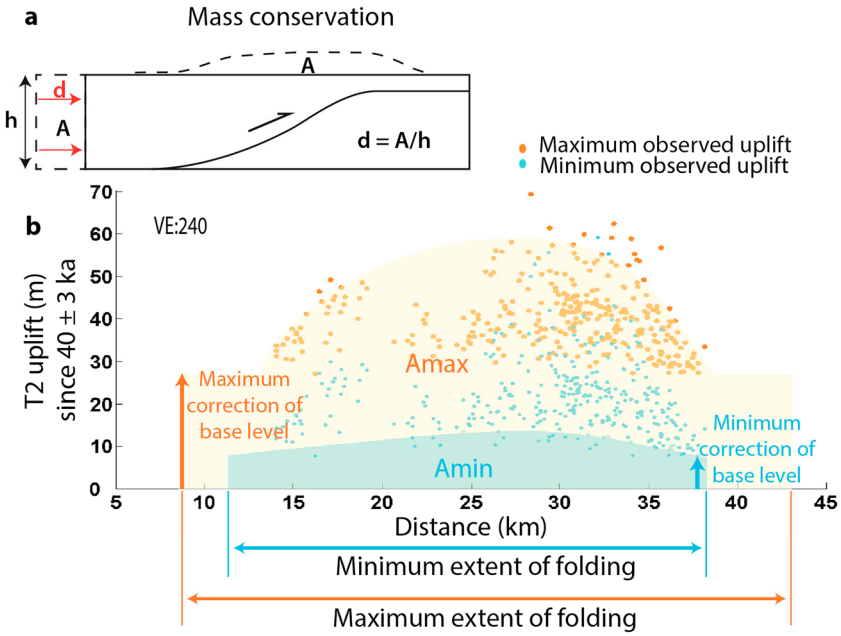


**Figure 10.** (a) Mass conservation principle (modified from Lavé & Avouac, 2000), used to derive incremental shortening. (b) Uplifted area as derived for terrace T2 and illustrating the contribution of sedimentation at the river base level. Minimum (blue) and maximum (yellow) values for the uplifted area used to derive incremental shortening according to Figure 10a are reported. See text for further details on our approach. The minimum and maximum extents of folding are defined in Figure 8. VE stands for vertical exaggeration. Dated terrace T2 is considered here as illustrative of our approach. Data for other terraces are reported in the supporting information (Figure S3).

horizontal extent of folding, defined as the horizontal distance separating the synclinal axis located just south of the Yecheng–Pishan fold from the first clearly nondeformed Cenozoic strata to the north of the fold (Figure 8).

The actual uplift pattern lies in between these minimum and maximum profiles, and our apparent uncertainties on the uplift integral *A* are large—but conservative—by following this approach. However, without further quantitative constraints on tectonic uplift where sedimentation prevails and on the sedimentation rate over the timescale of fluvial terraces, our conservative approach is the most appropriate and rigorous. We apply this approach to all the dated terraces (T2 and T4), as well as to those whose age is estimated by comparison to the paleoclimatic record of the Kesang Cave (T3, T5, and T6; Table 2, Figure S3 in the supporting information).

### 5.3. Slip Rate on the Blind Ramp Beneath the Yecheng–Pishan Fold

Using the uplift profiles, we derive incremental slip on the fault by assuming conservation of mass (equation (1), Figure 10a). We estimate the depth *h* of the decollement behind the fold to be 11 to 15 km from our structural cross section when corrected for the average altitude of the Keliyang River across the fold. The minimum and maximum uplifted areas *A* are then used to calculate the minimum and maximum incremental slip *d* on the fault since terrace formation. Table 2 reports the obtained results. Note that our approach based on the conservation of uplifted area does not make any particular assumption on which thrust ramps of the Yecheng–Pishan duplex are active.

**Table 2**
*Minimum and Maximum Uplifted Areas and Associated Minimal and Maximal Incremental Shortenings (Figures 10 and 11)*

| Terrace level | Minimum uplifted area ($m^2$) | Maximum uplifted area ($m^2$) | Minimum shortening (m) | Maximum shortening (m) |
|---|---|---|---|---|
| T2 | $3.0 \times 10^5$ | $15.2 \times 10^5$ | 13 | 126 |
| T3 | $6.9 \times 10^5$ | $33.4 \times 10^5$ | 29 | 276 |
| T4 | $13.3 \times 10^5$ | $65.1 \times 10^5$ | 56 | 538 |
| T5 | $21.6 \times 10^5$ | $96.2 \times 10^5$ | 96 | 797 |
| T6 | $30.5 \times 10^5$ | $121.8 \times 10^5$ | 143 | 1010 |

We compare the calculated minimum and maximum incremental slip to the actual age of terraces T2 to T6 (Table 1) and find a linear correlation between incremental slip and terrace age (given our large uncertainties), suggesting a slip rate of 0.5 to 2.5 mm/yr (Figure 11). It should be noted that we can only define minimum and maximum slip rates across the Yecheng–Pishan fold and not an average value with a statistically meaningful uncertainty. In addition, we do not find any particular difference when deriving the slip rate from dated

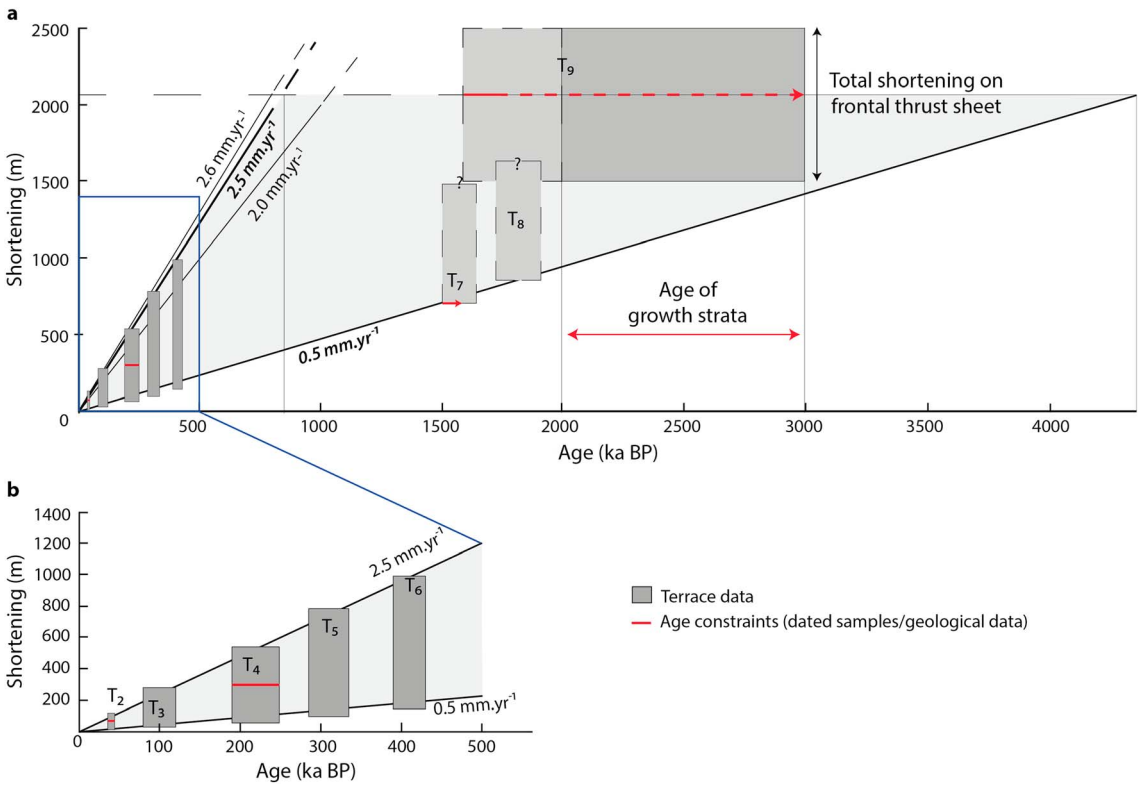


**Figure 11.** (a) Cumulative shortening on the frontal thrust sheet of the Yecheng–Pishan fold over time, as derived from uplifted terraces and growth strata. (b) Close-up view on cumulative shortening on this frontal thrust sheet over the last ~500 kyr from terrace data. Cumulative shortening of terraces is derived from the mass conservation approach illustrated in Figure 10a, and total shortening on the foremost frontal thrust sheet is retrieved from our geological cross section (Figure 6). Ages are either obtained by dating (red data) or by interpreting terraces as related to a wetter regional climate (Figure 5). The age of the oldest growth strata at the front of the foremost thrust sheet is retrieved from the cross section and from the ages of seismic horizons (Figure 6—see text for further details). Few constraints exist on the cumulative shortening and chronology of terraces T7, T8, and T9. It may be proposed that the T9 terrace roughly corresponds to the oldest growth strata on the frontal thrust sheet, dating initiation of deformation and uplift. A slip rate of 0.5 to 2.5 mm/yr is proposed from terrace data, from a conservative approach accounting for minimum and maximum cumulative shortenings, consistent with constraints from growth strata. This value on the frontal thrust sheet compares well with the total long-term value of 2 to 2.6 mm/yr retrieved across the four thrust sheets at the scale of the whole Yecheng–Pishan fold (Figure 6).

terraces only or from all the terraces, either dated or with estimated ages (Figure 11). This result also supports our interpretation on the climate-related formation of the studied terraces—at least for T2 to T6—and on their ages as proposed from the regional paleoclimatic record of the Kesang Cave (Figure 5). Finally, the slip rate of 0.5 to 2.5 mm/yr obtained over the last ~400–500 kyr from terraces T2 to T6 is also similar to the 0.8 to 1.1 and 2 to 2.6 mm/yr shortening rate values derived from our geological cross section over the last 2–3 Myr and 5.5–7 Myr, respectively.

## 6. Discussion

### 6.1. Limits and Uncertainties on the Estimated Fault Slip Rate

#### 6.1.1. Uncertainties Related to Our Structural Interpretation

By using a mass conservation approach to derive the fault slip rate on the blind ramp beneath the Yecheng–Pishan fold, our slip rate estimate depends neither on the details of the structural geometry of the active fault(s) nor on the folding mechanism (Figure 10a). This estimate is only built upon the hypothesis of plain strain and upon knowledge of the depth of the deeper decollement behind the fold.

We do not observe any particular evidence for strike-slip faulting over our study site, which would have questioned the plain strain hypothesis (Figure 7). The Yecheng–Pishan fold shows structural variations along strike, in particular with two anticlines in its westernmost portion (C. Y. Wang et al., 2013) simplifying into one single anticline at our study site (T. Li et al., 2016; R. Lu et al., 2016; Figure 4). It is possible that the normal faults mapped along the forelimb and oblique to the main fold axis absorb such structural lateral variations (Figure 7). We cannot therefore exclude the fact that folding and deformation may not be purely

cylindrical over our whole study site. However, the deformation recorded by remnants of the same relative terrace levels showed to the first order a similar and continuous pattern along strike when combined together, whatever their initial valley across the fold (Figure 9). Second-order discrepancies to this observation showed a systematic pattern, rather related to the initial geomorphology of our study site than to eventual east–west lateral structural variations: indeed, incision appeared systematically lower by up to ~50 m within the valleys of the inner channels R2 and R3 than within the ones of the outer channels R1 and R4. We therefore believe that any possible departure from plain strain is accounted for by our large and conservative uncertainties.

The depth of the decollement behind the fold is constrained from the structural interpretation of a seismic profile running across our study site (Figures 6 and 8). Other cross sections of the Yecheng–Pishan fold have been published within the same area (T. Li et al., 2016; R. Lu et al., 2016) or farther west (C. Y. Wang et al., 2013). These interpretations are similar to ours in terms of general structural style. However, when getting into details, the previous interpretations suggest that the blind frontal ramp and associated decollements lie at a depth either shallower or deeper by a few kilometers than that estimated here. We believe that these discrepancies relate to the different seismic velocities used for the depth conversion of seismic profiles. For example, T. Li et al. (2016) report a uniform velocity of 3,000 m $s^{-1}$, a value quite low for terrigenous and carbonaceous sediments buried to a depth of several kilometers. Because we take particular care on the depth conversion of our seismic profile by using seismic velocity constraints from well measurements (Table S1; (Laborde, 2017)), we feel confident on our structural results. Due to this, we also favor our own estimate on the cumulative shortening of the foremost thrust sheet of 1.5 to 2.5 km, slightly lower than the 2 km (R. Lu et al., 2016) to 3 km (T. Li et al., 2016) proposed by others along the same section.

Overall, we propose a cross section in which shortening accommodated by duplexing within the Yecheng–Pishan fold is transferred to the Mazar Tagh along the Paleogene decollement (Figure 6). This interpretation is overall similar to that of R. Lu et al. (2016) and accounts for the northward vergence of the Mazar Tagh, the rooting of this thrust into the Paleogene shallow marine series and the absence of evidence for passive roof backthrust atop the Yecheng–Pishan duplex. The large dimensions of the Mazar Tagh thrust sheet (Figures 4 and 6) favor the idea that this structure is major and that it therefore probably absorbed a significant amount of shortening. Because topographic relief is limited at the Mazar Tagh, this suggests that, on the long-term, erosion has been significant enough above this thrust ramp to remove the total 14 to 15 km of shortening transferred from the Yecheng–Pishan fold. It should be noted here that such significant long-term erosion was most probably operated by migrating paleo-rivers crossing the Tarim Basin (J. Pan et al., 2010; Yang et al., 2002) and only applies locally above the thrust ramp and within former river valleys. It should not be confused with the observed limited erosion of preserved planar geomorphic surfaces, such as the fluvial terraces investigated and dated here.

Therefore, taken altogether and given our geological, chronological, and morphological observations, we believe our structural interpretation is reasonable and realistic.

#### 6.1.2. Uncertainties Related to Our Geomorphological Analysis

Incremental uplift is estimated from the pattern of terrace incision across the fold by correcting for sedimentation at the river base level. A sedimentation rate of 0.2 to 0.6 mm/yr is deduced from the thickness of the Plio-Quaternary seismic interval on the seismic profile (Figures 6 and 8). This value is however lower than published regional estimates (Métivier & Gaudemer, 1997) or than that deduced from magnetostratigraphic sections (Zheng et al., 2000). The sedimentation rate of 0.5 to 1 mm/yr proposed by Métivier and Gaudemer (1997) along the topographic mountain front was obtained by interpolating data only from six drill holes across the whole Tarim Basin and therefore only provided a first-order estimate. The magnetostratigraphic section of (Zheng et al. 2000) also supports a higher sedimentation rate of ~1 mm/yr. However, this section has been obtained immediately south of Yecheng within the bend between the Western Kunlun and eastern Pamir ranges, where sediment thicknesses (and therefore sedimentation rates) are known to be highest (Métivier & Gaudemer, 1997). Moreover, the recent revision of the magnetostratigraphic ages (Zheng et al., 2015) demonstrates that this value has to be considered with caution. The value of ~1 mm/yr should therefore be considered as a maximum of the rate of base level change within our study area. Our sedimentation rate of 0.2 to 0.6 mm/yr seems therefore reasonable for our case study.

This sedimentation rate is retrieved over a long period (~5 Myr) that integrates several shorter-term fluctuations in the river base level, such as those of climatic origin at the timescale of river terrace formation. If we take the paleoclimatic record of regional moisture from the Kesang Cave (H. Cheng et al., 2012), several arid and relatively wetter periods have alternated over the last 500 kyr. The topmost alluvial fan and older river terraces have therefore integrated several climatic variations and possibly several climatically related fluctuations of the river base level, in contrast with the youngest terraces. Because sedimentation contributes to ~50% to 75% of the terrace uplift relative to incision, any major variation in the sedimentation rate at the timescale of terrace formation would alter significantly our results. However, we do not find any particular discrepancy between the results obtained from our different terraces, either from the youngest or the ones possibly as old as 400–500 ka (Figure 11). We therefore believe our long-term sedimentation rate to be representative of the sedimentation rate at the timescale of mapped river terraces, at least within the large uncertainties (50%) we arbitrarily ascribe to this rate.

The slip rate obtained by our approach also depends on the ages of the terraces, since finite sedimentation and uplift estimates are both dependent on these ages. As explained previously, we chose to ascribe to T4 the age of 220 ± 30 ka instead of 255 ± 35 ka because of its better fit with the paleoclimatic record of the Kesang Cave (Figure 5) and of the reasonable hypothesis on negligible surface erosion over this timescale. However, we do not expect this choice to have a significant impact on our results. Indeed, when using the age of 255 ± 35 ka for T4, the retrieved incision rate along the fold axis decreases to ~0.15 mm/yr. Such decrease in incision only represents ~10% of the terrace uplift pattern at most, so that any uncertainty related to the age of T4 should be accounted by the large uncertainties ascribed to our results.

#### 6.1.3. Comparing Our Fault Slip Rate to Existing Estimates

Our morphological analysis of the Yecheng–Pishan fold suggests a slip rate of 0.5 to 2.5 mm/yr over the last 400–500 kyr on the blind ramp(s) beneath the fold. Our structural cross section across the fold and over the southern half of the Tarim Basin suggests that any slip on the Yecheng–Pishan blind ramp is transferred onto the Paleogene decollement to the deformation front at the Mazar Tagh. A slip rate of 0.9 mm/yr has been proposed for the thrust ramp breaking the surface at the Mazar Tagh based on a fluvial terrace with a supposed age of ~50–160 ka (J. Pan et al., 2010). This value is consistent with our findings from the Yecheng–Pishan fold, even though on the lower range. Avouac et al. (1993) estimated a minimum crustal shortening rate of 4.5 ± 3 mm/yr over the last ~17 kyr across the Western Kunlun by interpreting the vertical throw rate of normal faults nearby Qira (east of the Western Kunlun range) as representative of the flexural subsidence of the Tarim Basin due to the overthrusting range. This value is also consistent with our findings, even though in the higher range. This could be due to the existence of other active faults absorbing crustal shortening across the Western Kunlun, such as the Tiekelik thrust fault (Figure 1). However, the estimate of Avouac et al. (1993) probably needs to be revised with new constraints on the subsidence and underthrusting of the Tarim Basin, on the geometry of structures at depth, and on the actual ages of investigated terraces. We do not know of any other direct estimate of fault slip rates in the Western Kunlun mountain range at the timescale of several seismic cycles (tens to hundreds of kiloyears); our study therefore provides the first well-constrained data of this kind.

Over a longer timescale, our estimate over the last ~500 kyr compares also relatively well with the value of 2 to 2.6 mm/yr obtained from our cross section across the whole Yecheng–Pishan duplex. Further east, a relatively similar long-term shortening rate of 2.4 and 1.6 mm/yr has been proposed by (Jiang, Li, & Li, 2013) across the Sanju and Pianamen folds, respectively, to the southwest of the town of Hotan. These latter values were derived from the total cumulative shortening retrieved by retrodeforming geological cross sections and assuming an age of deformation inception of ~23 Ma. Please note that we correct here the 0.2 mm/yr rate proposed by these authors across the Pianamen fold into a 1.6 mm/yr rate, by accounting for the total shortening of 37 km from their retrodeformed section (supporting information of Jiang, Li, & Li, 2013) rather than the value of 24.6 km referred in the main manuscript. Over a slightly shorter timescale, our shortening rate of 0.8 to 1.1 mm/yr on the sole most frontal thrust sheet is consistent with the minimum 0.8 mm/yr rate proposed by T. Li et al. (2016) on the same structure. Overall, these long-term shortening rate estimates are similar—but in the higher range—to our findings for the Yecheng–Pishan fold over a shorter timescale of ~500 kyr. Only long-term estimates on the sole frontal thrust of the Yecheng–Pishan fold tend to be in the lower range of our shorter-term estimates. This will be further commented hereafter. In any case, this overall consistency over various timescales and when compared to other independent results supports our findings.

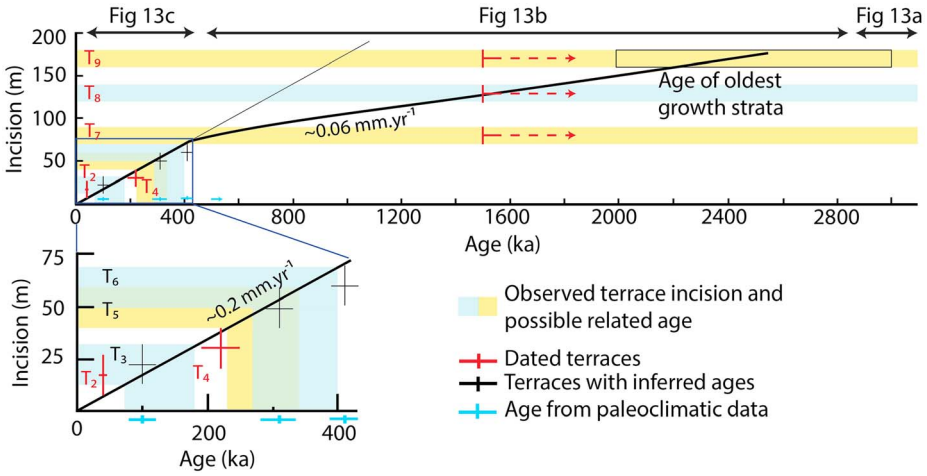


**Figure 12.** River incision over time, as derived from the altitude of terrace remnants preserved along the fold axis in valleys R2 and R3. A close-up view is proposed over the last 400 kyr for easier reading. Red crosses represent the incision and age constraints for dated terraces T2 and T4. An incision rate of ~0.2 mm/yr is deduced from these data. Other data (black crosses) indicate the incision of other nondated terraces, with age constraints as deduced from our climatic interpretation of terraces (Figure 5). These age values compare well with those that can be deduced from the actual incision of these terraces and the incision rate of ~0.2 mm/yr (yellow and blue areas). A lower incision rate may have prevailed during the early folding history (before 400 ka) as the rate of 0.2 mm/yr is not consistent with existing constraints on oldest terraces T7, T8, and T9. An earlier incision rate of ~0.06 mm/yr is proposed by dating T9 with the age of the oldest growth strata observed at the front of the foremost thrust sheet in our cross section. Black arrows at the top indicate the time period considered for sketches in Figure 13.

### 6.2. Structural and Morphological Evolution of Our Study Site

From our morphological analysis of the Yecheng–Pishan fold, we find a 0.5 to 2.5 mm/yr shortening and fault slip rate over the last ~400 to 500 kyr. Compared to the underlying structures, the morphology of uplifted terraces and fan surfaces suggests that the present-day morphology is mainly related to slip on its sole frontal thrust ramp (Figure 8). Indeed, deformation and slip on the penultimate ramp would have induced uplift and incision within the southern fan surfaces at the rear of the present-day fold, a pattern presently not observed (Figure 8).

Figure 12 reports incision of the different terrace and fan surfaces together with their age. To make the comparison easier, we only consider the maximum incision of these surfaces along the fold axis, within inner channels R2 and R3 where these surfaces are best preserved. Age constraints on T2 and T4, together with age estimates proposed for T3, T5, and T6, indicate a maximum ~0.2 mm/yr incision rate (Figure 12). However, incision is expected to have been much lower prior to T6, given the minimum age of 1.5 Ma derived from in situ produced $^{10}$Be for T7 and T9 (Table 1). This is particularly verified if T9 is interpreted as the surface of a former alluvial fan abandoned when deformation initiated on the underlying frontal thrust, that is, most probably by 2 to 3 Ma as deduced from growth strata. We interpret this increase in the long-term incision rate as related to an increase in tectonic uplift between T7 and T6 (i.e., sometime between ~1.5 Ma and ~400 ka) on the most frontal and recent thrust of the Yecheng–Pishan duplex. We suggest that this increase in tectonic uplift is the result of the probable progressive transfer of deformation from the penultimate to the most frontal thrust ramp (Figure 13).

From these simple observations, we propose a scenario for the long-term structural and morphological evolution of the Yecheng–Pishan fold nearby Pishan (Figure 13). Duplexing initiated by 5.5–7 Ma with a long-term shortening rate of 2 to 2.6 mm/yr. Before ~2–3 Ma, three thrust sheets had already been accreted (Figure 13a). A large fan had formed downstream from the deforming and uplifted area. Although the seismic profile shows probable erosional surfaces above the duplex, we have no real constraints on the precise timing and morphology during accretion of each one of these initial three thrust sheets. By ~2–3 Ma, deformation initiated on the present-day foremost thrust, leading to incision of the previous fan and to the formation of surface T9 (Figure 13b). However, from ~2–3 Ma to ~400–500 ka, deformation was probably partitioned between the two most frontal thrust sheets, with a progressive transfer of the overall 2 to 2.6 mm/yr shortening rate from the penultimate to the most recent thrust (Figure 13b). During this transitional period, the uplift rate above the foremost thrust was probably not much higher than the

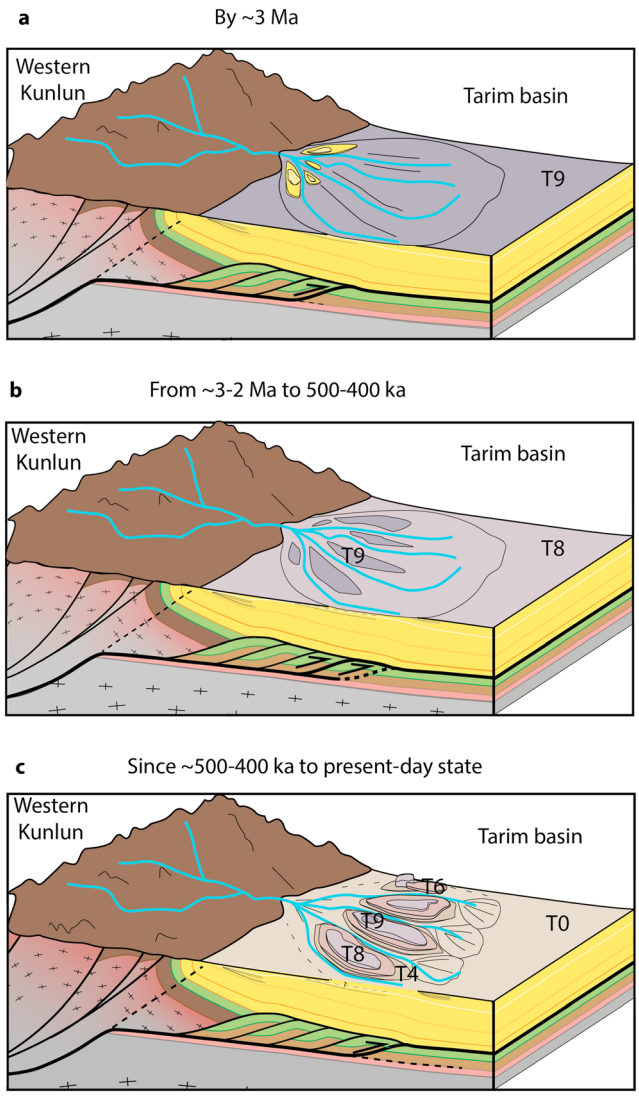


**Figure 13.** Morphological evolution of the Yecheng–Pishan fold in relation to the structural evolution of the most frontal thrust sheet. Three main stages are illustrated: (a) right before deformation inception on the foremost thrust by 3 Ma, (b) after initiation of deformation on this frontal thrust and during a probable period of partitioning of deformation between the two most frontal thrusts from 2 Ma to ~400–500 ka, and (c) the situation since ~400 ka with shortening only on the frontal thrust. Note that surface morphology and structures at depth do not follow the same vertical scale, for illustrative reasons.

sedimentation rate, inducing limited incision and preservation of the probable initial terraces (Figure 12). By ~400 ka, deformation had probably stopped on the penultimate thrust, so that all of the 2 to 2.6 mm/yr shortening rate was finally taken up by slip on the sole foremost thrust. At that time, uplift and incision rates increased by the present-day Yecheng–Pishan fold, leading to the current fold morphology above the frontal thrust (Figure 13c). Such a structural and morphological scenario suggests that the shortening rate of 2 to 2.6 mm/yr across the whole duplex system has been steady over the long-term (since ~5.5–7 Ma). Overall, from this geomorphological and structural interpretation of the Yecheng–Pishan fold, we favor the higher range of slip rate values retrieved from our analysis of incised terraces and fans and refine our estimate of 0.5 to 2.5 mm/yr to a most probable value of 2 to 2.5 mm/yr.

### 6.3. Implications in Terms of Seismic Hazards Within the Region

#### 6.3.1. Seismotectonic Context of the 2015 Pishan Earthquake

As explained previously, we follow previous authors (T. Li et al., 2016; R. Lu et al., 2016) and interpret the 3 July 2015 Pishan earthquake ($M_w$ 6.4) as the rupture of the frontal blind ramp beneath our study site (Figures 6 and 8). The rupture remained at depth (He et al., 2016; Wen et al., 2016) and probably did not propagate much into the structural flat of the Paleogene shallow decollement to the front of the Yecheng–Pishan fold. The structural context of this earthquake is analogous to that of the 2013 $M_w$ 6.6 Lushan earthquake along the mountain front of the LongMen Shan range (Y. Li et al., 2014) or to that of the 2015 $M_w$ 7.9 Gorkha earthquake in Nepal, except that this latter Himalayan earthquake did not rupture the midcrustal ramp located beneath the high Himalayan peaks but the flat upper decollement nearby the ramp (e.g., Grandin, Vallée, & Satriano, 2015). Therefore, despite their differences in terms of magnitude and energy release, these three earthquakes only ruptured the deeper part of a basal decollement below the associated mountain ranges, leaving slip deficit on their shallower and frontal basal thrusts. Such slip deficit is to be released in future earthquakes in the case that the shallower basal thrust is seismically locked.

An average coseismic slip of ~40 cm on a ~40 km by ~20 km patch has been estimated for the Pishan earthquake from the modeling of coseismic surface deformation derived from InSAR (He et al., 2016; Wen et al., 2016). Based on these values and in the case that this patch was fully locked and coupled prior to the earthquake and considering a long-term slip rate of ~2 to 2.5 mm/yr on the basal decollement, a time interval of ~160–200 years is needed to accumulate a slip deficit equivalent to the estimated average coseismic displacement. Global earthquake catalogues may not be complete prior to 1950, and we do not know of any historical earthquake archives within the Tarim region. The last known earthquakes of similar magnitudes in this area are the ones of the 4 June 1952 ($M_w$ 5.8) and 5 March 1956 ($M_w$ 6.1) to the east and west of the 2015 coseismic patch, respectively (Figure 2). Therefore, the two events from the 1950s and the 2015 Pishan earthquake did not rupture the exact same fault patch, but different portions of the same fault system along strike, at a similar structural position. Given the distance separating the epicenters of these three events (~50 to 80 km), we do not expect any major overlap between the coseismic patches of these various earthquakes. The actual recurrence time of $M_w \geq 6$ earthquakes on the same fault patch is therefore longer than the ~60 years time interval between the 1950s earthquakes and the 2015 event, consistent with a probable recurrence time of ~160–200 years of $M_w \geq 6$ events on the same fault patch. In the case that the upper crustal ramp beneath the Yecheng–Pishan fold is only partially locked, this recurrence time would only be a minimum.

#### 6.3.2. Potential Seismic Hazards Associated With the Paleogene Decollement Beneath the Southern Tarim

From our structural and morphological analysis of the Yecheng–Pishan fold, we determine a slip rate on the ramp beneath the fold and consequently on the Paleogene decollement that extends from the Western Kunlun topographic front to the Mazar Tagh. This slip rate, which is estimated over a period of ~400 kyr and therefore integrates slip over several seismic cycles, ranges from 0.5 to 2.5 mm/yr, with a most probable value of 2 to 2.5 mm/yr (Figure 11). However, how this rate is accommodated over a shorter timescale, that is, whether or not the slip is absorbed seismically or aseismically, is of major relevance for regional seismic hazards.

Presently, deformation across the Western Kunlun range and the Tarim Basin is recorded by GPS (Figures 2 and 3). These geodetic data indicate a shortening rate of at most 5 mm/yr across the whole region and according to our structural and morphological estimates, most probably within the GPS measurement uncertainties. To the south, GPS surface displacements within the interior of the mountain range seem indeed systematically higher than those measured within the footwall of the Paleogene decollement across the Tarim, to the north of the Mazar Tagh (Figure 3). This probable north–south gradient in GPS displacements is not documented as precisely as needed to be interpreted either as related to creep on this decollement released toward the surface at the Mazar Tagh or as the locking and interseismic elastic loading of its shallow portion. In the former case, crustal strain is continuously released by creep and does not build up sufficiently to generate major earthquakes. In the case of interseismic locking and loading, the shallow portion of the decollement is locked and cumulates elastic strain that is released during subsequent earthquakes. If this were the case, the dimensions of the locked portion of the decollement are critical to estimate the magnitudes of potential earthquakes.

If the Paleogene decollement reaching the surface at the Mazar Tagh is continuously creeping and releasing strain over the short term, low magnitude earthquakes could be expected to have been recorded over the whole southern Tarim. However, as mentioned previously, this region has recorded very little seismicity (Figures 2 and 3). Seismicity is indeed localized along the Western Kunlun mountain front and within the mountain range, along the frontal folds and nearby the Altyn Tagh–Karakax Fault. This seismicity is therefore structurally controlled (Figure 3). These observations in the Western Kunlun are somehow analogous to observations made in the Himalayas of central Nepal (e.g., Ader et al., 2012; Bollinger et al., 2004; Cattin & Avouac, 2000; Grandin et al., 2012). There, microseismicity is essentially recorded around the midcrustal ramp beneath the high Himalayan peaks. In particular, the location of this microseismicity coincides with the transition from the deep creeping to the shallow locked portion of the basal decollement of the Himalayan range and has been interpreted as related to the stress buildup at this transition (Bollinger et al., 2004; Cattin & Avouac, 2000). Given the similarities between the Western Kunlun and the Himalayas of central Nepal in terms of seismicity distribution and possible gradient in horizontal GPS velocities relative to geological structures (Figure 3), together with the interpretation proposed in the Himalayan case, we give some preferentiality to the idea that the Paleogene decollement beneath the southern Tarim Basin could be locked at short interseismic timescales, probably over a large distance of ~180 km, from the blind ramp beneath the topographic front up to the Mazar Tagh frontal ramp.

We explore the idea that the whole Paleogene decollement is locked from the blind ramp beneath the Western Kunlun mountain front up to the Mazar Tagh. We estimate the two-dimensional potency rate $P$ (integral of slip rate over the fault area—e.g., Simoes, Avouac, & Chen, 2007) on the basal decollement in the case that it is fully locked, from

$$P = W \cdot v \tag{2}$$

with $W$ the width of the locked fault from its surface trace at the Mazar Tagh down to the probable edge of the deep creeping zone beneath the mountain front folds and $v$ the slip rate estimated here. Using the fault slip rate estimated here (Figure 11) and a locked fault width of 180 km (Figures 3−4 and 6), we find a potency rate of ~360–450 $m^2$/yr. Given the large dimensions (~300 km × 180 km) of the probable locked patch, megaearthquakes of magnitudes $M_w \geq 8$ are to be expected in the case that the large Paleogene decollement releases accumulated strain in one single seismic event. The two-dimensional potency of such events would be $\geq 7.2 \times 10^5$ $m^2$. When compared to the 2-D potency rate previously estimated, a minimum recurrence time of ~1.6 to 2 kyr for such major events is found. In the case that the basal decollement is only partially locked

and/or that it ruptures during earthquakes of smaller magnitudes ($M_w$ ~5–7), such megaevents would be even more rare, but not impossible. A better appraisal of the seismic hazards in this region is therefore needed. Historical and archeological archives could be useful to trace past earthquakes, even though the abandonment of former settlements has been usually ascribed to climatic variability rather than to earthquakes (Debaine-Francfort, 2001; Debaine-Francfort, Debaine, & Idriss, 2009).

Large magnitude earthquakes breaking low dip angle decollements are not rare. Several examples exist in the case of the Himalayas, such as in the case of the recent 2015 Gorkha earthquake (e.g., Elliott et al., 2016; Grandin, Vallée, & Satriano, 2015) or in the case of mega-earthquakes rupturing the whole Main Himalayan Thrust up to the surface such as in 1934 (Sapkota et al., 2012). Interseismic locking of this shallow decollement may seem surprising because it is embedded into series of the Paleogene Kashgar Group containing some evaporites. Indeed, such lithologies have a reputably low friction coefficient and frequently locate major regional decollements: the Jura mountain ranges along the frontal western European Alps (East France) rooting into Triassic gypsum or the Zagros decollement embedded into the Hormuz salt are some well-known examples (e.g., Affolter, 2004; McQuarrie, 2004; Sepehr & Cosgrove, 2004; Sommaruga, 1999). However, such low friction coefficient defines the long-term mechanical behavior of evaporites. It may not be representative of the shorter-term mechanical properties of such lithologies, in particular at the timescale of one single seismic cycle. Over the short-term, some studies suggest that evaporitic decollements may creep and not store elastic strain, based on the comparison between short- and long-term distributions of shortening across the Zagros of Iran (Oveisi et al., 2009) or from the modeling of GPS data across the Salt Ranges of Pakistan (Jouanne et al., 2014). However, in these contexts, thicknesses of the sedimentary series containing evaporites are significantly higher than within the Tarim Basin (~up to >1 km versus a 250 m at most of evaporites, interlayered with limestones, sandstones, and claystones in our case). At the front of the LongMen Shan range, the thin evaporitic Triassic detachment within the Sichuan Basin (Hubbard, Shaw, & Klinger, 2010; Y. Li et al., 2014) is a better analog to the Paleogene decollement within the Tarim Basin. This detachment is also reputably aseismic, but essentially because of the poor knowledge of historical and paleoseismological earthquake record (Hubbard, Shaw, & Klinger, 2010). Moreover, several studies have documented earthquakes rupturing faults embedded in evaporitic sequences such as the Triassic evaporitic decollement at the front of the Long-Men Shan (2013 Lushan earthquake; Y. Li et al., 2014) and in other tectonic contexts (e.g., De Paola et al., 2008; Mirabella et al., 2008). Back to a more regional perspective, the 1985 $M_w$ 7.4 Wuqia earthquake along the Eastern Pamir mountain front, which is thought to have ruptured part of the Tuomuluoan Thrust rooted into Paleogene gypsum (Feng, 1994; T. Li, Chen, et al., 2012; Wang, Cheng, Chen, Ding, et al., 2016), could be a possible illustration of potential earthquakes rupturing faults imbedded in such lithologies. Further constraints on the seismic or aseismic behavior of such decollement levels, according to their precise lithologies and thicknesses, are thus needed, in particular when laboratory experiments on rock deformation suggest the possibility of frictional seismic instabilities for sequences of carbonates and evaporites at seismogenic depths (Collettini, De Paola, & Faulkner, 2009; Scuderi, Niemeijer, & Collettini, 2013).

## 7. Conclusion

In this study, we conduct a detailed structural and morphological analysis of the Yecheng–Pishan fold near the 2015 $M_w$ 6.4 Pishan earthquake epicenter and find nine levels of incised fluvial terraces and alluvial fans. From their incision pattern and using age constraints available on some of these terraces, we are able to quantify the slip rate on the underlying blind frontal ramp to 0.5 to 2.5 mm/yr, with a most probable value between 2 and 2.5 mm/yr when compared to the long-term kinematics of the fold. The evolution of the Yecheng–Pishan fold is then proposed by combining all structural, morphological, and chronological observations.

From our detailed analysis of a seismic profile running across the epicentral region of the Pishan earthquake and over the southern Tarim Basin, we assess the geological and structural context of this earthquake and propose that the blind ramp that ruptured during the Pishan event connects to the Mazar Tagh thrust in the central Tarim Basin through a decollement within Paleogene shallow marine series, containing some evaporites. By comparing the seismotectonic context of this earthquake to the Himalayas of Central Nepal, we propose that the Pishan event could be an intermediate earthquake rupturing only the deeper portion of the basal decollement and that major events with $M \geq 8$ could occur in the case that the whole

decollement across the southern Tarim ruptures in one single event, from the topographic mountain front all the way up to the Mazar Tagh. Such mega-earthquakes would be rare with recurrence periods over 1.6 to 2 kyr. Such a scenario implies that the whole decollement is locked during the interseismic period, which needs to be verified to get further insights into the seismic hazards of this slowly deforming intracontinental mountain range.

**Acknowledgments**
The investigations presented in this manuscript were conducted with research grants from the INSU-CNRS RELIEF (M.S.) and SYSTER (L.B.) programs and from the IPGP BQR program (M.S.) as well as from the China Geological Survey grant DD20160022 (H.L.). C.G. benefitted from a Master financial support from IPGP. C.G., A.L., and T.C. benefitted from a PhD grant from the French Ministry of Research and Higher Education (MESR). $^{10}$Be accelerator mass spectrometry measurements were performed at ASTER French national facility in CEREGE (Centre Européen de Recherche et d'Enseignement des Géosciences de l'Environnement, Aix-en-Provence) supported by the University Aix-Marseille, the French Ministry of Research and Higher Education (MESR), the Commissariat à l'Energie Atomique (CEA), and the Institut National des Sciences de l'Univers/Centre National de la Recherche Scientifique (INSU/CNRS). We also thank LHyGeS (UMR 7517 CNRS/Université de Strasbourg) and particularly the Laboratoire de Chimie Isotopique in Strasbourg (France) for access to various facilities, and R. Boutin for ICP-MS measurements. J. Pan and A. Lorne participated in the fieldwork and particularly in the sampling for cosmogenic isotopic dating. These data can be found in the supporting information. The seismic data used for this study are a courtesy of the Sinopec Group of the China Petrochemical Corporation. A. Delorme (IPGP) is thanked for his help in ortho-rectifying SPOT images. The thorough reviews by J. Hollingsworth and J. Thompson-Jobe were much appreciated and helped improve the content and presentation of this manuscript. This is IPGP contribution 3907.

## References

Abdrakhmatov, K. Y., Aldazhanov, S. A., & Hager, B. H. (1996). Relatively recent construction of the Tien Shan inferred from GPS measurements of present-day crustal deformation rates. *Nature, 384*(6608), 450–453. https://doi.org/10.1038/384450a0

Ader, T., Avouac, J. P., Liu-Zeng, J., Lyon-Caen, H., Bollinger, L., Galetzka, J., … Flouzat, M. (2012). Convergence rate across the Nepal Himalaya and interseismic coupling on the main Himalayan thrust: Implications for seismic hazard. *Journal of Geophysical Research*, *117*, B04403. https://doi.org/10.1029/2011JB009071

Affolter, T. (2004). Map view retrodeformation of an arcuate fold-and-thrust belt: The Jura case. *Journal of Geophysical Research*, *109*, B03404. https://doi.org/10.1029/2002JB002270

Aizen, V. B., Aizen, E. M., Joswiak, D. R., & Fujita, K. (2006). Climatic and atmospheric circulation pattern variability from ice-core isotope/geochemistry records (Altai, Tien Shan and Tibet). *Annals of Glaciology*, *43*(1), 49–60. https://doi.org/10.3189/172756406781812078

Armijo, R., Rauld, R., Thiele, R., Vargas, G., Campos, J., Lacassin, R., & Kausel, E. (2010). The West Andean Thrust, the San Ramón Fault, and the seismic hazard for Santiago, Chile. *Tectonics*, *29*, TC2007. https://doi.org/10.1029/2008TC002427

Avouac, J. P., Tapponnier, P., Bai, M., You, H., & Wang, G. (1993). Active thrusting and folding along the northern Tien Shan and Late Cenozoic rotation of the Tarim relative to Dzungaria and Kazakhstan. *Journal of Geophysical Research*, *98*(B4), 6755–6804. https://doi.org/10.1029/92JB01963

Balco, G., Stone, J. O., Lifton, N. A., & Dunai, T. J. (2008). A complete and easily accessible means of calculating surface exposure ages or erosion rates from $^{10}$Be and $^{26}$Al measurements. *Quaternary Geochronology*, *3*(3), 174–195. https://doi.org/10.1016/j.quageo.2007.12.001

Barberà, X., Cabrera, L., Marzo, M., & Parés, J. M. (2001). A complete terrestrial Oligocene magnetobiostratigraphy from the Ebro Basin, Spain. *Earth and Planetary Science Letters*, *187*(1-2), 1–16. https://doi.org/10.1016/S0012-821X(01)00270-9

Barrientos, S. E., & Ward, S. N. (1990). The 1960 Chile earthquake: Inversion for slip distribution from surface deformation. *Geophysical Journal International*, *103*(3), 589–598. https://doi.org/10.1111/j.1365-246X.1990.tb05673.x

Berger, A. L. (1978). Long-term variations of caloric insolation resulting from the Earth's orbital elements. *Quaternary Research*, *9*(02), 139–167. https://doi.org/10.1016/0033-5894(78)90064-9

Bilham, R., Gaur, V. K., & Molnar, P. (2001). Himalayan seismic hazard. *Science*, *633*, 34–42. https://doi.org/10.1016/j.tecto.2014.06.031

Bollinger, L., Avouac, J. P., Beyssac, O., Catlos, E. J., Harrison, T. M., Grove, M., … Sapkota, S. (2004). Thermal structure and exhumation history of the Lesser Himalaya in central Nepal. *Tectonics*, *23*, TC5015. https://doi.org/10.1029/2003TC001564

Bollinger, L., Tapponnier, P., Sapkota, S. N., & Klinger, Y. (2016). Slip deficit in central Nepal: Omen for a repeat of the 1344 AD earthquake? *Earth, Planets and Space*, *68*(1), 12. https://doi.org/10.1186/s40623-016-0389-1

Bonini, M. (2001). Passive roof thrusting and forelandward fold propagation in scaled brittle–ductile physical models of thrust wedges. *Journal of Geophysical Research*, *106*(B2), 2291–2311. https://doi.org/10.1029/2000JB900310

Bonnet, C., Malavieille, J., & Mosar, J. (2007). Interactions between tectonics, erosion, and sedimentation during the recent evolution of the Alpine orogen: Analogue modeling insights. *Tectonics*, *26*, TC6016. https://doi.org/10.1029/2006TC002048

Bosboom, R., Dupont-Nivet, G., Grothe, A., Brinkhuis, H., Villa, G., Mandic, O., … Krijgsman, W. (2014). Linking Tarim Basin sea retreat (west China) and Asian aridification in the late Eocene. *Basin Research*, *26*(5), 621–640. https://doi.org/10.1111/bre.12054

Brown, E. T., Edmond, J. M., Raisbeck, G. M., & Yiou, F. (1991). Examination of surface exposure ages of Antarctic moraines using in situ produced $^{10}$Be and $^{26}$Al. *Geochimica et Cosmochimica Acta*, *55*(8), 2269–2283. https://doi.org/10.1016/0016-7037(91)90103-C

Bull, W. B. (1991). *Geomorphic responses to climatic change*. Oxford: Oxford University Press.

Burbank, D. W., & Anderson, R. S. (2011). *Tectonic geomorphology*. Hoboken, NJ: John Wiley. https://doi.org/10.1002/9781444345063

Burbank, D. W., Raynolds, R. G. H., & Johnson, G. D. (1986). Late Cenozoic tectonics and sedimentation in the north-western Himalayan foredeep: II. Eastern limb of the northwest syntaxis and regional synthesis. In *Foreland basins* (pp. 293–306). Oxford, UK: Blackwell Ltd. https://doi.org/10.1002/9781444303810.ch16

Cao, K., Wang, G.-C., Bernet, M., van der Beek, P., & Zhang, K.-X. (2015). Exhumation history of the west Kunlun mountains, northwestern Tibet: Evidence for a long-lived, rejuvenated orogen. *Earth and Planetary Science Letters*, *432*(C), 391–403. https://doi.org/10.1016/j.epsl.2015.10.033

Cattin, R., & Avouac, J. P. (2000). Modeling mountain building and the seismic cycle in the Himalaya of Nepal. *Journal of Geophysical Research*, *105*(B6), 13,389–13,407. https://doi.org/10.1029/2000JB900032

Charreau, J., Gumiaux, C., Avouac, J. P., & Augier, R. (2009). The Neogene Xiyu Formation, a diachronous prograding gravel wedge at front of the Tianshan: Climatic and tectonic implications. *Earth and Planetary Science Letters*, *287*(3-4), 298–310. https://doi.org/10.1016/j.epsl.2009.07.035

Chen, W.-S., Lee, K.-J., Lee, L.-S., Ponti, D. J., Prentice, C., Chen, Y.-G., … Lee, Y.-H. (2004). Paleoseismology of the Chelungpu Fault during the past 1900 years. *Quaternary International*, *115-116*, 167–176. https://doi.org/10.1016/S1040-6182(03)00105-8

Cheng, H., Zhang, P. Z., Spötl, C., Edwards, R. L., Cai, Y. J., Zhang, D. Z., … An, Z. S. (2012). The climatic cyclicity in semiarid-arid central Asia over the past 500,000 years. *Geophysical Research Letters*, *39*, L01705. https://doi.org/10.1029/2011GL050202

Cheng, X., Chen, H., Lin, X., Wu, L., & Gong, J. (2016). Geometry and kinematic evolution of the Hotan-Tiklik segment of the western Kunlun thrust belt: Constrained by structural analyses and apatite fission track thermochronology. *The Journal of Geology*, *125*(1), 65–82. https://doi.org/10.1086/689187

Chlieh, M., Avouac, J. P., Hjorleifsdottir, V., Song, T. R. A., Ji, C., Sieh, K., … Galetzka, J. (2007). Coseismic slip and afterslip of the great $M_w$ 9.15 Sumatra-Andaman earthquake of 2004. *Bulletin of the Seismological Society of America*, *97*(1A), S152–S173. https://doi.org/10.1785/0120050631

Collettini, C., De Paola, N., & Faulkner, D. R. (2009). Insights on the geometry and mechanics of the Umbria–Marche earthquakes (Central Italy) from the integration of field and laboratory data. *Tectonophysics*, *476*(1-2), 99–109. https://doi.org/10.1016/j.tecto.2008.08.013

De Paola, N., Collettini, C., Faulkner, D. R., & Trippetta, F. (2008). Fault zone architecture and deformation processes within evaporitic rocks in the upper crust. *Tectonics*, *27*, TC4017. https://doi.org/10.1029/2007TC002230

Debaine-Francfort, C. (2001). Keriya, mémoires d'un fleuve Archéologie et civilisation des oasis du Taklamakan Mission archéologique franco-chinoise au Xinjiang.

Debaine-Francfort, C., Debaine, F., & Idriss, A. (2009). The Taklimakan oases: An environmental evolution shown through geoarchaeology. In G. Schneier-Madanes & M.-F. Courel (Eds.), *Water and sustainability in arid regions* (pp. 181–202). Dordrecht, Netherlands: Springer.

Dominguez, S., Avouac, J.-P., & Michel, R. (2003). Horizontal coseismic deformation of the 1999 Chi-Chi earthquake measured from SPOT satellite images: Implications for the seismic cycle along the western foothills of central Taiwan, *Journal of Geophysical Research*, *108*(B2), 2083. https://doi.org/10.1029/2001JB000951

Dubille, M., & Lavé, J. (2015). Rapid grain size coarsening at sandstone/conglomerate transition: Similar expression in Himalayan modern rivers and Pliocene molasse deposits. *Basin Research*, *27*(1), 26–42. https://doi.org/10.1111/bre.12071

Elliott, J. R., Jolivet, R., González, P. J., Avouac, J. P., Hollingsworth, J., Searle, M. P., & Stevens, V. L. (2016). Himalayan megathrust geometry and relation to topography revealed by the Gorkha earthquake. *Nature Geoscience*, *9*(2), 174–180. https://doi.org/10.1038/ngeo2623

Feng, X. Y. (1994). *Surface rupture associated with the 1985 Wuqia earthquake* (pp. 45–55). Xinjiang: Research on Active Fault.

Fillon, C., Huismans, R. S., & Van Der Beek, P. (2012). Syntectonic sedimentation effects on the growth of fold-and-thrust belts. *Geology*, *41*(1), 83–86. https://doi.org/10.1130/G33531.1

Finnegan, N. J., & Dietrich, W. E. (2011). Episodic bedrock strath terrace formation due to meander migration and cutoff. *Geology*, *39*(2), 143–146. https://doi.org/10.1130/G31716.1

Fluteau, F., Ramstein, G., & Besse, J. (1999). Simulating the evolution of the Asian and African monsoons during the past 30 Myr using an atmospheric general circulation model. *Journal of Geophysical Research*, *104*(D10), 11,995–12,018. https://doi.org/10.1029/1999JD900048

Gan, W., Zhang, P., Shen, Z.-K., Niu, Z., Wang, M., Wan, Y., … Cheng, J. (2007). Present-day crustal motion within the Tibetan plateau inferred from GPS measurements. *Journal of Geophysical Research*, *112*, B08416. https://doi.org/10.1029/2005JB004120

Godard, V., Cattin, R., & Lavé, J. (2009). Erosional control on the dynamics of low-convergence rate continental plateau margins. *Geophysical Journal International*, *179*(2), 763–777. https://doi.org/10.1111/j.1365-246X.2009.04324.x

Gosse, J. C., & Phillips, F. M. (2001). Terrestrial in situ cosmogenic nuclides: Theory and application. *Quaternary Science Reviews*, *20*(14), 1475–1560. https://doi.org/10.1016/S0277-3791(00)00171-2

Grandin, R., Doin, M. P., Bollinger, L., Pinel-Puyssegur, B., Ducret, G., Jolivet, R., & Sapkota, S. N. (2012). Long-term growth of the Himalaya inferred from interseismic InSAR measurement. *Geology*, *40*(12), 1059–1062. https://doi.org/10.1130/G33154.1

Grandin, R., Vallée, M., & Satriano, C. (2015). Rupture process of the $M_w$ = 7.9 2015 Gorkha earthquake (Nepal): Insights into Himalayan megathrust segmentation. *Geophysical Research Letters*, *42*, 8373–8382. https://doi.org/10.1002/2015GL066044

Guan, S., He, D., Lei, Y., & Chen, Z. (2013). Kinematic classification, structural modeling and prospective fields of the foreland thrust belts in Midwest China. *Petroleum Exploration and Development*, *40*(1), 69–83. https://doi.org/10.1016/S1876-3804(13)60007-5

Guérin, G., Christophe, C., Philippe, A., Murray, A. S., Thomsen, K. J., Tribolo, C., … Lahaye, C. (2017). Absorbed dose, equivalent dose, measured dose rates, and implications for OSL age estimates: Introducing the average dose model. *Quaternary Geochronology*, *41*, 163–173. https://doi.org/10.1016/j.quageo.2017.04.002

Guérin, G., Discamps, E., Lahaye, C., & Mercier, N. (2012). Multi-method (TL and OSL), multi-material (quartz and flint) dating of the Mousterian site of Roc de Marsal (Dordogne, France): Correlating Neanderthal occupations with the climatic variability of MIS 5–3. *Journal of Archaeological Science*, *39*(10), 3071–3084. https://doi.org/10.1016/j.jas.2012.04.047

Guérin, G., Mercier, N., & Adamiec, G. (2011). Dose–rate conversion factors: Update. *Ancient TL*, *29*(1), 5–8.

Hansen, V., Murray, A., Buylaert, J.-P., Yeo, E.-Y., & Thomsen, K. (2015). A new irradiated quartz for beta source calibration. *Radiation Measurements*, *81*(C), 123–127. https://doi.org/10.1016/j.radmeas.2015.02.017

He, P., Wang, Q., Ding, K., Wang, M., Qiao, X., Li, J., … Zou, R. (2016). Source model of the 2015 $M_w$ 6.4 Pishan earthquake constrained by interferometric synthetic aperture radar and GPS: Insight into blind rupture in the western Kunlun Shan. *Geophysical Research Letters*, *43*, 1511–1519. https://doi.org/10.1002/2015GL067140

Heermance, R. V., Chen, J., Burbank, D. W., & Wang, C. (2007). Chronology and tectonic controls of Late Tertiary deposition in the southwestern Tian Shan foreland, NW China. *Basin Research*, *19*(4), 599–632. https://doi.org/10.1111/j.1365-2117.2007.00339.x

Hossler, T., Bollinger, L., Sapkota, S. N., Lavé, J., Gupta, R. M., & Kandel, T. P. (2016). Surface ruptures of large Himalayan earthquakes in western Nepal: Evidence along a reactivated strand of the Main Boundary Thrust. *Earth and Planetary Science Letters*, *434*(C), 187–196. https://doi.org/10.1016/j.epsl.2015.11.042

Hsu, Y. J., Yu, S. B., Simons, M., Kuo, L. C., & Chen, H. Y. (2009). Interseismic crustal deformation in the Taiwan plate boundary zone revealed by GPS observations, seismicity, and earthquake focal mechanisms. *Tectonophysics*, *479*(1-2), 4–18. https://doi.org/10.1016/j.tecto.2008.11.016

Huang, W.-L., Yang, X.-P., Li, A., Thompson, J. A., & Zhang, L. (2014). Climatically controlled formation of river terraces in a tectonically active region along the southern piedmont of the Tian Shan, NW China. *Geomorphology*, *220*, 15–29. https://doi.org/10.1016/j.geomorph.2014.05.024

Hubbard, J., & Shaw, J. H. (2009). Uplift of the Longmen Shan and Tibetan plateau, and the 2008 Wenchuan ($M$ = 7.9) earthquake. *Nature*, *458*(7235), 194–197. https://doi.org/10.1038/nature07837

Hubbard, J., Shaw, J. H., & Klinger, Y. (2010). Structural setting of the 2008 $M_w$ 7.9 Wenchuan, China, earthquake. *Bulletin of the Seismological Society of America*, *100*(5B), 2713–2735. https://doi.org/10.1785/0120090341

Jiang, X., Jin, Y., & McNutt, M. K. (2004). Lithospheric deformation beneath the Altyn Tagh and west Kunlun faults from recent gravity surveys. *Journal of Geophysical Research*, *109*, B05406. https://doi.org/10.1029/2003JB002444

Jiang, X., Li, Z. X., & Li, H. (2013). Uplift of the west Kunlun range, northern Tibetan plateau, dominated by brittle thickening of the upper crust. *Geology*, *41*(4), 439–442. https://doi.org/10.1130/G33890.1

Jiang, X. D., & Li, Z. X. (2014). Seismic reflection data support episodic and simultaneous growth of the Tibetan plateau since 25 Myr. *Nature Communications*, *5*, 5453. https://doi.org/10.1038/ncomms6453

Jin, X., Wang, J., Chen, B., & Ren, L. (2003). Cenozoic depositional sequences in the piedmont of the west Kunlun and their paleogeographic and tectonic implications. *Journal of Asian Earth Sciences*, *21*(7), 755–765. https://doi.org/10.1016/S1367-9120(02)00073-1

Jouanne, F., Awan, A., Pêcher, A., & Kausar, A. (2014). Present-day deformation of northern Pakistan from Salt Ranges to Karakorum ranges. *Journal of Geophysical Research: Solid Earth*, *119*, 2487–2503. https://doi.org/10.1002/2013JB010776

Kao, H., Gao, R., Rau, R.-J., Shi, D., Chen, R.-Y., Guan, Y., & Wu, F. T. (2001). Seismic image of the Tarim basin and its collision with Tibet. *Geology*, *29*(7), 575–578. https://doi.org/10.1130/0091-7613(2001)029%3C0575:SIOTTB%3E2.0.CO;2

Kohl, C. P., & Nishiizumi, K. (1992). Chemical isolation of quartz for measurement of in-situ-produced cosmogenic nuclides. *Geochimica et Cosmochimica Acta*, *56*(9), 3583–3587. https://doi.org/10.1016/0016-7037(92)90401-4

Laborde, A. (2017). Déformation cénozoïque du bassin du Tarim (Xinjiang, Chine) et impact sur son paysage morpho-sédimentaire actuel (PhD thesis). Paris: University Paris 7-IPGP. 29 September.

Lal, D. (1991). Cosmic ray labeling of erosion surfaces: In situ nuclide production rates and erosion models. *Earth and Planetary Science Letters*, *104*(2-4), 424–439. https://doi.org/10.1016/0012-821X(91)90220-C

Lavé, J. (2005). Evidence for a great medieval earthquake (1100 A.D.) in the central Himalayas, Nepal. *Science*, *307*(5713), 1302–1305. https://doi.org/10.1126/science.1104804

Lavé, J., & Avouac, J. P. (2000). Active folding of fluvial terraces across the Siwaliks Hills, Himalayas of central Nepal. *Journal of Geophysical Research*, *105*(B3), 5735–5770. https://doi.org/10.1029/1999JB900292

Li, D., Yue, Z., Hu, J., Wan, J., Li, X., Zhou, X., … Pei, J. (2007). Fission track thermochronologic constraints on plateau surface and geomorphic relief formation in the northwestern margin of the Tibetan plateau. *Acta Petrologica Sinica*, *23*, 900–910.

Li, D. S., Liang, D. G., & Jian, C. Z. (1996). *Hydrocarbon accumulations in the Tarim Basin*. China: AAPG Bulletin.

Li, Q., You, X., Yang, S., Du, R., Qiao, X., Zou, R., & Wang, Q. (2012). A precise velocity field of tectonic deformation in China as inferred from intensive GPS observations. *Science China Earth Sciences*, *55*(5), 695–698. https://doi.org/10.1007/s11430-012-4412-5

Li, T., Chen, J., Fang, L., Chen, Z., Thompson, J. A., & Jia, C. (2016). The 2015 $M_w$ 6.4 Pishan earthquake: Seismic hazards of an active blind wedge thrust system at the western Kunlun range front, northwest Tibetan plateau. *Seismological Research Letters*, *87*(3), 601–608. https://doi.org/10.1785/0220150205

Li, T., Chen, J., Thompson, J. A., Burbank, D. W., & Xiao, W. (2012). Equivalency of geologic and geodetic rates in contractional orogens: New insights from the Pamir frontal thrust. *Geophysical Research Letters*, *39*, L15305. https://doi.org/10.1029/2012GL051782

Li, T., Chen, J., Thompson, J. A., Burbank, D. W., & Yang, X. (2013). Quantification of three-dimensional folding using fluvial terraces: A case study from the Mushi anticline, northern margin of the Chinese Pamir. *Journal of Geophysical Research: Solid Earth*, *118*, 4628–4647. https://doi.org/10.1002/jgrb.50316

Li, Y., Jia, D., Wang, M., Shaw, J. H., He, J., Lin, A., … Rao, G. (2014). Structural geometry of the source region for the 2013 $M_w$ 6.6 Lushan earthquake: Implication for earthquake hazard assessment along the Longmen Shan. *Earth and Planetary Science Letters*, *390*(C), 275–286. https://doi.org/10.1016/j.epsl.2014.01.018

Lin, C., Yang, H., Liu, J., Rui, Z., Cai, Z., & Zhu, Y. (2012). Distribution and erosion of the Paleozoic tectonic unconformities in the Tarim Basin, northwest China: Significance for the evolution of paleo-uplifts and tectonic geography during deformation. *Journal of Asian Earth Sciences*, *46*(C), 1–19. https://doi.org/10.1016/j.jseaes.2011.10.004

Lu, H., Burbank, D. W., & Li, Y. (2010). Alluvial sequence in the north piedmont of the Chinese Tian Shan over the past 550 kyr and its relationship to climate change. *Palaeogeography, Palaeoclimatology, Palaeoecology*, *285*(3-4), 343–353. https://doi.org/10.1016/j.palaeo.2009.11.031

Lu, R., Xu, X., He, D., Liu, B., Tan, X., & Wang, X. (2016). Coseismic and blind fault of the 2015 Pishan $M_w$ 6.5 earthquake: Implications for the sedimentary-tectonic framework of the western Kunlun Mountains, northern Tibetan plateau. *Tectonics*, *35*, 956–964. https://doi.org/10.1002/2015TC004053

Lyon Caen, H., & Molnar, P. (1984). Gravity anomalies and the structure of western Tibet and the southern Tarim Basin. *Geophysical Research Letters*, *11*(12), 1251–1254. https://doi.org/10.1029/GL011i012p01251

Matte, P., Tapponnier, P., Arnaud, N., Bourjot, L., Avouac, J. P., Vidal, P., … Yi, W. (1996). Tectonics of western Tibet, between the Tarim and the Indus. *Earth and Planetary Science Letters*, *142*(3-4), 311–330. https://doi.org/10.1016/0012-821X(96)00086-6

Mattern, F., & Schneider, W. (2000). Suturing of the Proto-and Paleo-Tethys oceans in the western Kunlun (Xinjiang, China). *Journal of Asian Earth Sciences*, *18*(6), 637–650. https://doi.org/10.1016/S1367-9120(00)00011-0

McQuarrie, N. (2004). Crustal scale geometry of the Zagros fold–thrust belt, Iran. *Journal of Structural Geology*, *26*(3), 519–535. https://doi.org/10.1016/j.jsg.2003.08.009

Métivier, F., & Gaudemer, Y. (1997). Mass transfer between eastern Tien Shan and adjacent basins (central Asia): Constraints on regional tectonics and topography. *Geophysical Journal International*, *128*(1), 1–17. https://doi.org/10.1111/j.1365-246X.1997.tb04068.x

Milana, J. P., & Ruzycki, L. (1999). Alluvial-fan slope as a function of sediment transport efficiency. *Journal of Sedimentary Research*, *69*(3), 553–562. https://doi.org/10.2110/jsr.69.553

Milana, J. P., & Tietze, K.-W. (2002). Three-dimensional analogue modelling of an alluvial basin margin affected by hydrological cycles: Processes and resulting depositional sequences. *Basin Research*, *14*(3), 237–264. https://doi.org/10.1046/j.1365-2117.2002.00188.x

Mirabella, F., Barchi, M., Lupattelli, A., Stucchi, E., & Ciaccio, M. G. (2008). Insights on the seismogenic layer thickness from the upper crust structure of the Umbria-Marche Apennines (central Italy). *Tectonics*, *27*, TC1010. https://doi.org/10.1029/2007TC002134

Mugnier, J. L., Baby, P., Colletta, B., Vinour, P., Bale, P., & Leturmy, P. (1997). Thrust geometry controlled by erosion and sedimentation: A view from analogue models. *Geology*, *25*(5), 427–425. https://doi.org/10.1130/0091-7613(1997)025%3C0427:TGCBEA%3E2.3.CO;2

Murray, A. S. (1996). Developments in optically stimulated luminescence and photo-transferred thermoluminescence dating of young sediments: Application to a 2000-year sequence of flood deposits. *Geochimica et Cosmochimica Acta*, *60*(4), 565–576. https://doi.org/10.1016/0016-7037(95)00418-1

Murray, A. S., Marten, R., Johnston, A., & Martin, P. (1987). Analysis for naturally occuring radionuclides at environmental concentrations by gamma spectrometry. *Journal of Radioanalytical and Nuclear Chemistry Articles*, *115*(2), 263–288. https://doi.org/10.1007/BF02037443

Murray, A. S., Thomsen, K. J., Masuda, N., Buylaert, J. P., & Jain, M. (2012). Identifying well-bleached quartz using the different bleaching rates of quartz and feldspar luminescence signals. *Radiation Measurements*, *47*(9), 688–695. https://doi.org/10.1016/j.radmeas.2012.05.006

Murray, A. S., & Wintle, A. G. (2000). Luminescence dating of quartz using an improved single-aliquot regenerative-dose protocol. *Radiation Measurements*, *32*(1), 57–73. https://doi.org/10.1016/S1350-4487(99)00253-X

Murray, A. S., & Wintle, A. G. (2003). The single aliquot regenerative dose protocol: Potential for improvements in reliability. *Radiation Measurements*, *37*(4-5), 377–381. https://doi.org/10.1016/S1350-4487(03)00053-2

Oveisi, B., Lavé, J., van der Beek, P., Carcaillet, J., Benedetti, L., & Aubourg, C. (2009). Thick- and thin-skinned deformation rates in the central Zagros simple folded zone (Iran) indicated by displacement of geomorphic surfaces. *Geophysical Journal International*, *176*(2), 627–654. https://doi.org/10.1111/j.1365-246X.2008.04002.x

Pan, B., Burbank, D., Wang, Y., Wu, G., Li, J., & Guan, Q. (2003). A 900 k.y. record of strath terrace formation during glacial–interglacial transitions in northwest China. *Geology*, *31*(11), 957. https://doi.org/10.1130/g19685.1

Pan, J., Li, H., Sun, Z., Pei, J., & Si, J. (2010). Deformation features of the Mazartagh fold–thrust belt, south central Tarim basin and its tectonic significances, Dizhi Kexue. *Chinese Journal of Geology*, *45*, 1038–1056.

Poisson, B., & Avouac, J.-P. (2004). Holocene hydrological changes inferred from alluvial stream entrenchment in north Tian Shan (northwestern China). *The Journal of Geology*, *112*(2), 231–249. https://doi.org/10.1086/381659

Prescott, J. R., & Hutton, J. T. (1994). Cosmic ray contributions to dose rates for luminescence and ESR dating: Large depths and long-term time variations. *Radiation Measurements*, *23*(2-3), 497–500. https://doi.org/10.1016/1350-4487(94)90086-8

Qiusheng, L., Rui, G., Deyuan, L., & Jingwei, L. (2002). Tarim underthrust beneath western Kunlun: Evidence from wide-angle seismic sounding. *Journal of Asian Earth Sciences*, *20*(3), 247–253. https://doi.org/10.1016/S1367-9120(01)00057-8

Railsback, L. B., Gibbard, P. L., Head, M. J., Voarintsoa, N. R. G., & Toucanne, S. (2015). An optimized scheme of lettered marine isotope substages for the last 1.0 million years, and the climatostratigraphic nature of isotope stages and substages. *Quaternary Science Reviews*, *111*, 94–106. https://doi.org/10.1016/j.quascirev.2015.01.012

Ramstein, G., Fluteau, F., Besse, J., & Joussaume, S. (1997). Effect of orogeny, plate motion and land–sea distribution on Eurasian climate change over the past 30 million years. *Nature*, *93*(2), 161–178. https://doi.org/10.1016/S0016-7878(82)80039-4

Reigber, C., Michel, G. W., Galas, R., & Angermann, D. (2001). New space geodetic constraints on the distribution of deformation in Central Asia. *Earth and Planetary Science Letters*, *191*(1-2), 157–165. https://doi.org/10.1016/S0012-821X(01)00414-9

Riesner, M., Lacassin, R., Simoes, M., Armijo, R., Rauld, R., & Vargas, G. (2017). Kinematics of the active west Andean fold-and-thrust belt (Central Chile): Structure and long-term shortening rate. *Tectonics*, *36*(2), 287–303. https://doi.org/10.1002/2016TC004269

Sapkota, S. N., Bollinger, L., Klinger, Y., Tapponnier, P., Gaudemer, Y., & Tiwari, D. (2012). Primary surface ruptures of the great Himalayan earthquakes in 1934 and 1255. *Nature Geoscience*, 1–10. https://doi.org/10.1038/ngeo1669

Scuderi, M. M., Niemeijer, A. R., & Collettini, C. (2013). Frictional properties and slip stability of active faults within carbonate–evaporite sequences: The role of dolomite and anhydrite. *Earth and Planetary Science Letters*, *369-370*, 220–232. https://doi.org/10.1016/j.epsl.2013.03.024

Sepehr, M., & Cosgrove, J. W. (2004). Structural framework of the Zagros fold–thrust belt, Iran. *Marine and Petroleum Geology*, *21*(7), 829–843. https://doi.org/10.1016/j.marpetgeo.2003.07.006

Simoes, M., & Avouac, J.-P. (2006). Investigating the kinematics of mountain building in Taiwan from the spatiotemporal evolution of the foreland basin and western foothills. *Journal of Geophysical Research*, *111*, B10401. https://doi.org/10.1029/2005JB004209

Simoes, M., Avouac, J.-P., & Chen, Y.-G. (2007). Slip rates on the Chelungpu and Chushiang thrust faults inferred from a deformed strath terrace along the Dungpuna river, west central Taiwan. *Journal of Geophysical Research*, *112*, B03S10. https://doi.org/10.1029/2005JB004200

Simoes, M., Chen, Y. G., & Shinde, D. P. (2014). Lateral variations in the long-term slip rate of the Chelungpu fault, Central Taiwan, from the analysis of deformed fluvial terraces. *Journal of Geophysical Research: Solid Earth*, *119*, 3740–3766. https://doi.org/10.1002/2013JB010057

Simons, M., Minson, S. E., Sladen, A., Ortega, F., Jiang, J., Owen, S. E., … Webb, F. H. (2011). The 2011 magnitude 9.0 Tohoku-Oki earthquake: Mosaicking the megathrust from seconds to centuries. *Science*, *332*(6036), 1421–1425. https://doi.org/10.1126/science.1206731

Sobel, E. R., & Arnaud, N. (1999). A possible middle Paleozoic suture in the Altyn Tagh, NW China. *Tectonics*, *18*(1), 64–74. https://doi.org/10.1029/1998TC900023

Sommaruga, A. (1999). Décollement tectonics in the Jura forelandfold-and-thrust belt. *Marine and Petroleum Geology*, *16*(2), 111–134. https://doi.org/10.1016/S0264-8172(98)00068-3

Stone, J. O. (2000). Air pressure and cosmogenic isotope production. *Journal of Geophysical Research*, *105*(B10), 23,753–23,759. https://doi.org/10.1029/2000JB900181

Sun, J. (2006). The age of the Taklimakan Desert. *Science*, *312*(5780), 1621–1621. https://doi.org/10.1126/science.1124616

Suppe, J., Wang, X., He, D., & Liang, H. (2015). Large-scale thrusting along the northern margin of the Tibetan plateau and the southwest Tarim basin: 230 km long active Hotian thrust sheet. Abstract T21A-2790 Presented at the 2015 AGU Fall Meeting, San Francisco, CA.

Thompson Jobe, J. A., Li, T., Chen, J., Burbank, D. W., & Bufe, A. (2017). Quaternary tectonic evolution of the Pamir-Tian Shan convergence zone, Northwest China. *Tectonics*, *36*. https://doi.org/10.1002/2017TC004541

Thompson, T. B., Plesch, A., Shaw, J. H., & Meade, B. J. (2015). Rapid slip-deficit rates at the eastern margin of the Tibetan plateau prior to the 2008 $M_w$7.9 Wenchuan earthquake. *Geophysical Research Letters*, *42*, 1677–1684. https://doi.org/10.1002/2014GL062833

Thomsen, K. J., Murray, A. S., Buylaert, J. P., Jain, M., Hansen, J. H., & Aubry, T. (2016). Testing single-grain quartz OSL methods using sediment samples with independent age control from the Bordes-Fitte rockshelter (Roches d'Abilly site, Central France). *Quaternary Geochronology*, *31*(C), 77–96. https://doi.org/10.1016/j.quageo.2015.11.002

Tong, D., Zhang, J., Yang, H., Hu, D., & Ren, J. (2012). Fault system, deformation style and development mechanism of the Bachu uplift, Tarim basin. *Journal of Earth Science*, *23*(4), 529–541. https://doi.org/10.1007/s12583-012-0273-2

Vargas, G., Klinger, Y., Rockwell, T. K., Forman, S. L., Rebolledo, S., Baize, S., … Armijo, R. (2014). Probing large intraplate earthquakes at the west flank of the Andes. *Geology*, *42*(12), 1083–1086. https://doi.org/10.1130/G35741.1

Vigny, C., Socquet, A., Peyrat, S., Ruegg, J. C., Metois, M., Madariaga, R., … Kendrick, E. (2011). The 2010 $M_w$ 8.8 Maule megathrust earthquake of Central Chile, monitored by GPS. *Science*, *332*(6036), 1417–1421. https://doi.org/10.1126/science.1204132

Wang, C., Cheng, X., Chen, H., Ding, W., Lin, X., Wu, L., … Li, Y. (2016). The effect of foreland palaeo-uplift on deformation mechanism in the Wupoer fold-and-thrust belt, NE Pamir: Constraints from analogue modelling. *Journal of Geodynamics*, *100*, 115–129. https://doi.org/10.1016/j.jog.2016.03.001

Wang, C., Cheng, X.-G., Chen, H.-L., Li, K., Fan, X.-G., & Wang, C.-Y. (2016). From folding to transpressional faulting: The Cenozoic Fusha structural belt in front of the western Kunlun Orogen, northwestern Tibetan plateau. *International Journal of Earth Sciences*, *105*(5), 1621–1636. https://doi.org/10.1007/s00531-016-1305-4

Wang, C., Dai, J., Zhao, X., Li, Y., Graham, S. A., He, D., … Meng, J. (2014). Outward-growth of the Tibetan plateau during the Cenozoic: A review. *Tectonophysics*, *621*(C), 1–43. https://doi.org/10.1016/j.tecto.2014.01.036

Wang, C.-Y., Chen, H.-L., Cheng, X.-G., & Li, K. (2013). Evaluating the role of syn-thrusting sedimentation and interaction with frictional detachment in the structural evolution of the SW Tarim basin, NW China: Insights from analogue modeling. *Tectonophysics*, *608*(C), 642–652. https://doi.org/10.1016/j.tecto.2013.08.016

Wang, E. (2003). Late Cenozoic geological evolution of the foreland basin bordering the west Kunlun range in Pulu area: Constraints on timing of uplift of northern margin of the Tibetan plateau. *Journal of Geophysical Research*, *108*(B8), 2401. https://doi.org/10.1029/2002JB001877

Wang, H., Liu, M., Cao, J., Shen, X., & Zhang, G. (2011). Slip rates and seismic moment deficits on major active faults in mainland China. *Journal of Geophysical Research*, *116*, B02405. https://doi.org/10.1029/2010JB007821

Wang, Q., Zhang, P. Z., Freymueller, J. T., Bilham, R., Larson, K. M., Lai, X. A., … Chen, Q. (2001). Present-day crustal deformation in China constrained by global positioning system measurements. *Science*, *294*(5542), 574–577. https://doi.org/10.1126/science.1063647

Wei, H.-H., Meng, Q.-R., Ding, L., & Li, Z.-Y. (2013). Tertiary evolution of the western Tarim basin, northwest China: A tectono-sedimentary response to northward indentation of the Pamir salient. *Tectonics*, *32*, 558–575. https://doi.org/10.1002/tect.20046

Wen, Y., Xu, C., Liu, Y., & Jiang, G. (2016). Deformation and source parameters of the 2015 $M_w$ 6.5 earthquake in Pishan, western China, from Sentinel-1A and ALOS-2 data. *Remote Sensing*, *8*(2), 134–114. https://doi.org/10.3390/rs8020134

Whipple, K. X., & Tucker, G. E. (1999). Dynamics of the stream-power river incision model: Implications for height limits of mountain ranges, landscape response timescales, and research needs. *Journal of Geophysical Research*, *104*(B8), 17,661–17,674. https://doi.org/10.1029/1999JB900120

Wittlinger, G., Vergne, J., Tapponnier, P., Farra, V., Poupinet, G., Jiang, M., … Paul, A. (2004). Teleseismic imaging of subducting lithosphere and Moho offsets beneath western Tibet. *Earth and Planetary Science Letters*, *221*(1-4), 117–130. https://doi.org/10.1016/S0012-821X(03)00723-4

Yang, X., Preusser, F., & Radtke, U. (2006). Late Quaternary environmental changes in the Taklamakan Desert, western China, inferred from OSL-dated lacustrine and aeolian deposits. *Quaternary Science Reviews*, *25*(9-10), 923–932. https://doi.org/10.1016/j.quascirev.2005.06.008

Yang, X., Scuderi, L., Paillou, P., Liu, Z., Li, H., & Ren, X. (2011). Quaternary environmental changes in the drylands of China—A critical review. *Quaternary Science Reviews*, *30*(23-24), 3219–3233. https://doi.org/10.1016/j.quascirev.2011.08.009

Yang, X., & Scuderi, L. A. (2010). Hydrological and climatic changes in deserts of China since the late Pleistocene. *Quaternary Research*, *73*(01), 1–9. https://doi.org/10.1016/j.yqres.2009.10.011

Yang, X., Zhu, Z., Jaekel, D., Owen, L. A., & Han, J. (2002). Late Quaternary palaeoenvironment change and landscape evolution along the Keriya River, Xinjiang, China: The relationship between high mountain glaciation and landscape evolution in foreland desert regions. *Quaternary International*, *97-98*, 155–166. https://doi.org/10.1016/S1040-6182(02)00061-7

Zhang, P.-Z., Shen, Z., Wang, M., Gan, W., Bürgmann, R., Molnar, P., … Xinzhao, Y. (2004). Continuous deformation of the Tibetan plateau from global positioning system data. *Geology*, *32*(9), 809–804. https://doi.org/10.1130/G20554.1

Zheng, D. (1999). *Physical-geography of the Karakorum-Kunlun Mountains*. Beijing: Science Press.

Zheng, H., Huang, X., & Butcher, K. (2006). Lithostratigraphy, petrography and facies analysis of the late Cenozoic sediments in the foreland basin of the west Kunlun. *Palaeogeography, Palaeoclimatology, Palaeoecology*, *241*, 61–78. https://doi.org/10.1016/j.palaeo.2006.06.015

Zheng, H., Powell, C. M., An, Z., Zhou, J., & Dong, G. (2000). Pliocene uplift of the northern Tibetan plateau. *Geology*, *28*(8), 715–718. https://doi.org/10.1130/0091-7613(2000)28%3C715:PUOTNT%3E2.0.CO;2

Zheng, H., Wei, X., Tada, R., Clift, P. D., Wang, B., Jourdan, F., … He, M. (2015). Late Oligocene–early Miocene birth of the Taklimakan Desert. *Proceedings of the National Academy of Sciences of the United States of America*, *112*(25), 7662–7667. https://doi.org/10.1073/pnas.1424487112

Zhu, Z. D., Wu, Z., Liu, S., & Di, X. (1980). *An outline of Chinese deserts*. Beijing: Science Press.

Zubovich, A. V., Wang, X.q., Scherba, Y. G., Schelochkov, G. G., Reilinger, R., Reigber, C., … Beisenbaev, R. T. (2010). GPS velocity field for the Tien Shan and surrounding regions. *Tectonics*, *29*, TC6014. https://doi.org/10.1029/2010TC002772